Journal of South American Earth Sciences 129 (2023) 104521

Contents lists available at ScienceDirect

Journal of South American Earth Sciences

journal homepage: www.elsevier.com/locate/jsames

Along-strike tectonic evolution of the Neogene Bermejo foreland basin and Eastern Precordillera thrust front, Argentina (30-32°S)

Zoey C. Plonka [a], Tomas N. Capaldi [a,*], Margaret L. Odlum [a], Chelsea Mackaman-Lofland [b], Gustavo Ortiz [c], Patricia Alvarado [c]

[a] Department of Geoscience, University of Nevada, Las Vegas, 4505 Maryland Parkway, Las Vegas, NV, 89154, USA
[b] Department of Earth and Environmental Sciences, Denison University, 100 W College St, Granville, OH, 43023, USA
[c] Conicet and Universidad Nacional de San Juan (CIGEOBIO), Departmento de Geofisica y Astronomía, FCEFN-UNSJ, Meglioli 1160 S, San Juan, Argentina

ARTICLE INFO

Keywords:
Andes
Argentina
Broken foreland basin
Bermejo basin
Stratigraphy
Fluvial mega-fan
Zircon U–Pb geochronology
Apatite (U–Th-Sm)/He thermochronology
Thermal history modeling

ABSTRACT

The Bermejo retroarc foreland basin system formed in flexural response to Cenozoic crustal thickening in the Andean orogenic system, specifically, the eastward propagation of the Precordillera fold-thrust belt and the basement-involved uplift of the Sierras Pampeanas. Previous work in the region has mainly focused on the mechanisms and expression of flat slab subduction and the structural geometry of the basement-involved Sierras Pampeanas and east-directed Precordillera fold-thrust belt at depth, advancing our understanding of the Bermejo basin history north of 31°S. However, the along strike evolution of the basin system to the south remains unresolved and contrasting tectonic models have proposed the Bermejo basin evolved synchronously versus asynchronously through time. Our study seeks to constrain the along-strike Neogene tectonics of the Bermejo basin via well-exposed Miocene fluvial stratigraphic intervals along the Eastern Precordillera, integrated with detrital zircon U–Pb geochronology provenance and detrital apatite (U–Th)/He thermochronology datasets. New data from two Neogene stratigraphic sections in the southern Bermejo basin constrain deposition between 13 and 6 Ma. Dominant fluvial-lacustrine mudstones, siltstones, and sandstones transition into fluvial-megafan deposits capped by alluvial fan conglomerate facies, tracking the eastward migration of Precordillera deformation. The cessation of sedimentation, and thermal history models of apatite (U–Th-Sm)/He thermochronology ages, indicates basin incorporation into the orogenic wedge by 6 Ma. When we compare our southern datasets with previous constraints from the northern Bermejo basin, we observe, from north to south: (1) a time-transgressive trend in basin initiation, (2) a ~3 km decrease in stratigraphic thicknesses, and (3) older exhumation along the thrust front. These trends highlight the asynchronous nature of the Bermejo foreland basin system and along-strike variability of Precordillera thrust-front evolution.

1. Introduction

The southern central Andean orogenic system is located within the Pampean flat slab region where the Nazca plate is subducted subhorizontally below the South American plate (Fig. 1; Barazangi and Isacks, 1976,1979; Ramos et al., 2002). This region of flat-slab subduction is recognized by a spatial gap of active arc magmatism that has been suggested to be driven largely by subduction of the Juan Fernandez ridge island chain associated with a mantle plume hot spot off the coast of Chile (Fig. 1; Barazangi and Isacks, 1976; Jordan et al., 1983; Ramos et al., 2002; Alvarado et al., 2009; Ramos and Folguera, 2009). Geophysical modeling of the Juan Fernandez ridge suggests that the asperity migrated south along the South American margin for the past 25 Myr, arriving at its current position (32°S) by 12 Ma (Yáñez et al., 2001; Kay and Coira, 2009). Andean deformation propagated eastward during the past ~35 Myr and was co-located with migration of magmatism towards the craton as the Nazca slab shallowed and induced thermal weaknesses in the overriding continental lithosphere (Jordan et al., 1983; Kay and Abbruzzi, 1996; Cristallini and Ramos, 2000; Kay and Mpodozis, 2001; Ramos et al., 2002; Ramos and Folguera, 2009; Allmendinger and Judge, 2014; Fosdick et al., 2015, 2017; Capaldi et al., 2021; Mackaman-Lofland et al., 2020, 2022). The late Miocene to recent shortening within the Sierras Pampeanas basement-involved ranges partitioned the once continuous foreland basin forming the modern

* Corresponding author.
E-mail address: tcapaldi@utexas.edu (T.N. Capaldi).

https://doi.org/10.1016/j.jsames.2023.104521
Received 15 May 2023; Received in revised form 24 July 2023; Accepted 31 July 2023
Available online 4 August 2023

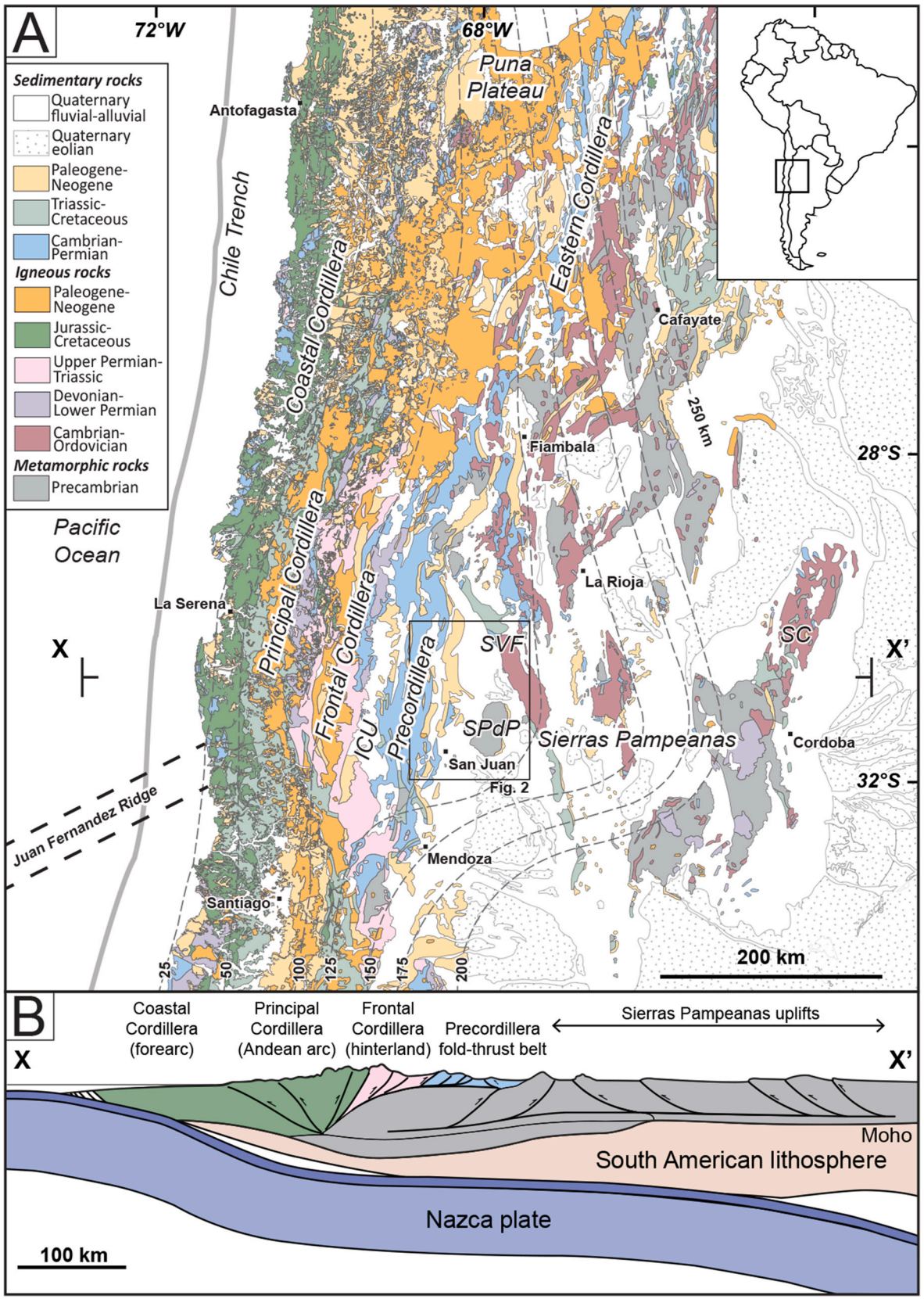

Fig. 1. Tectonic setting of the southern Central Andes. (A) Geologic map of major tectonic provinces in the Pampean flat-slab segment of western Argentina and northern Chile, contoured Benioff zone depths (in km) to the subducted Nazca plate (dashed contour lines), and cross- section X -X′ location (Ramos et al., 2002; Servicio Geológico Minero, 1999, 2012; Servicio Nacional de Geología, 2003). ICU: Iglesia-Calingasta-Uspallata basin; SC: Sierra Cordoba; SPdP: Sierra Pie de Palo; SVF: Sierra Valle Fertíl (B) East-west crustal and lithospheric cross section of the South American and Nazca plates (after Bellahsen et al., 2016).

broken foreland basin configuration (Fig. 1; Jordan and Allmendinger, 1986; Malizia et al., 1995; Jordan, 1995; Horton et al., 2022a). Research in the Pampean flat-slab region has advanced our understanding of the drivers and consequences of flat slab subduction at convergent plate boundaries, the development and evolution of broken-foreland basin systems, and the utility of well-preserved basin stratigraphy in understanding Andean tectonics. Nevertheless, the along strike trends in Bermejo foreland basin development and subsequent thrust front propagation remain unresolved.

The Cenozoic basin stratigraphy of the northern Bermejo basin (30–31°S) is a well-documented record of deformation in the Andean hinterland and Precordillera fold-thrust belt since 20 Ma (Johnson et al., 1986; Beer and Jordan, 1989; Jordan et al., 1993, 1997, 2001; Fernandez and Jordan, 1996; Milana et al., 2003; Capaldi et al., 2020; Stevens-Goddard et al., 2020; Mackaman-Lofland et al., 2022). Uncertainties remain with regards to the spatial and temporal along-strike evolution of deformation and associated foreland basin development. Andean mountain building has been proposed to be asynchronous from

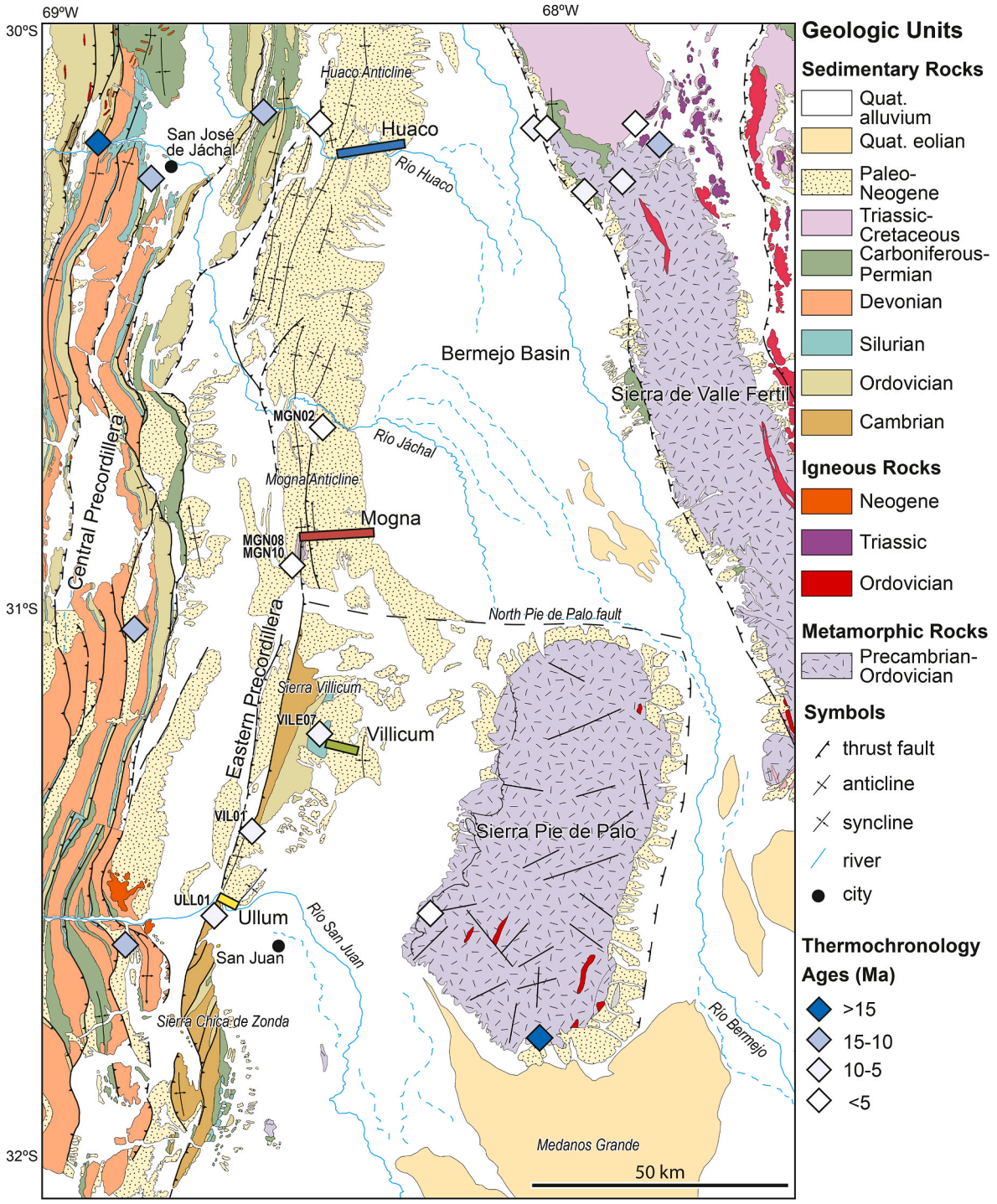

Fig. 2. Geologic map of the Bermejo broken foreland study area (modified from Ramos et al., 2000; Furque et al., 2003). Stratigraphic sections shown in colored rectangles. Published and new low-temperature apatite (U–Th-Sm)/He cooling ages shown in colored diamonds with new samples labeled (Löbens et al., 2013; Levina et al., 2014; Fosdick et al., 2015; Ortiz et al., 2015, 2021).

north to south, indicating deformation and foreland basin development tracks spatially and temporally with the subduction of the Juan Fernandez ridge and associated flat slab geometry (Beer and Jordan, 1989; Jordan et al., 1993, 2001; Ramos and Folguera, 2009; Vergés et al., 2001). However, low-temperature thermochronology results along the Precordillera fold-thrust belt suggest a synchronous exhumation history over an along-strike distance >100 km (Levina et al., 2014; Suriano et al., 2017; Buelow et al., 2018).

The Precordillera is subdivided into three zones. The Western and Central Precordillera comprise an east-directed, thin-skinned fold-thrust belt, while the Eastern Precordillera consists of a west-directed frontal thrust system (Fig. 2; Von Gosen, 1992). Reconstructions of the tectonic history of the Eastern Precordillera show large uncertainties in the initiation of deformation along strike, and the kinematic relationships between the Central Precordillera ramp-flat thrust system and the east flanking Sierras Pampeanas basement-involved uplifts. Integrated analysis of the depositional and deformational history between 30 and 32°S is crucial to understanding the variability that exists in the evolution of the Andean orogenic system and the development of the associated foreland basins.

Our study seeks to constrain the along-strike Neogene tectonics of the Bermejo basin and Eastern Precordillera through new stratigraphy, detrital zircon U–Pb geochronology, and detrital apatite (U–Th-Sm)/He thermochronology datasets from the southern Bermejo basin (Fig. 2). Temporal constraints in the northern Bermejo basin suggest deposition initiated around 24-18 Ma (Johnson et al., 1986; Milana et al., 2003) and between 20 and 7 Ma the basin strata thickened progressively towards the west in a simple foreland wedge (Jordan et al., 2001). By 6 Ma, the basin geometry had become more symmetrical, with the greatest thickness in the center of the Bermejo Valley. By 2 Ma, exhumation of the basin deposits occurred during incorporation into the orogenic wedge above the Eastern Precordillera (Fosdick et al., 2015; Mackaman-Lofland et al., 2022). We integrate new datasets from the southern Bermejo basin with previous constraints from northern Bermejo basin localities to assess whether: (1) the Bermejo basin developed as a continuous flexural basin or was spatially discontinuous along strike, and (2) shortening-induced exhumation of basin deposits was coeval or diachronous along strike. We strive to establish regional continuity of these trends where they have only previously been explored in the northern Bermejo basin to track the along-strike variations and complexities in thrust-front evolution and foreland basin development.

2. Geologic Background

The Andean foreland of west-central Argentina is located within the Pampean flat slab segment of the Nazca-South American plate boundary, where the thin-skinned Precordillera and thick-skinned (basement-involved) Sierras Pampeanas structural provinces spatially overlap (Fig. 1; Jordan and Allmendinger, 1986; Horton et al., 2022a). Many fold-thrust belts exhibit a continuum of thin- and thick-skinned structural styles (e.g., Pfiffner, 2017; Butler et al., 2018; Parker and Pearson, 2021). Thin-skinned thrust belts exhibit ramp-flat geometries that are rooted within a décollement in sedimentary cover strata, and are typically detached from the underlying crystalline basement (Boyer, 1995). Thick-skinned tectonics are defined by the involvement of basement in deformation, commonly along high-angle ramps that may reach mid-crustal levels (Erslev, 1993; Lacombe and Bellahsen, 2016).

The south-central Andes (30–32°S) is divided into five distinct tectonic provinces (Figs. 1 and 2) from west to east: (1) the Andean arc and hinterland, (2) Western and Central Precordillera, (3) Eastern Precordillera, (4) Sierras Pampeanas, and (5) Bermejo foreland basin. The Andean arc and hinterland region along the Chile-Argentina border is composed of Triassic-Miocene volcanic, volcaniclastic, and sedimentary rocks. These rocks are deformed within the thin-skinned Principal Cordillera fold-thrust belt and depositionally overlie the Frontal Cordillera domain (Fig. 1; Cristallini and Ramos, 2000; Mackaman-Lofland et al., 2019). The Frontal Cordillera is characterized by a series of high-angle thrust faults that exhumed a >3 km thick assemblage of largely Carboniferous-Triassic igneous rocks that define the regional mechanical basement (Heredia et al., 2002; Lossada et al., 2017; Mackaman-Lofland et al., 2022; Bertoa del Llano et al., in review). Igneous rocks of the Frontal Cordillera include the Elqui-Limarí and Chollay batholiths, Choiyoi Group granodiorites, andesitic/rhyolitic lavas, and pyroclastic rocks (Mpodozis and Kay, 1992; Sato et al., 2015). The Manantiales and Iglesia-Calingasta-Uspallata hinterland basins within and along the Frontal Cordillera record deposition from ~22 to 14 Ma (Pinto et al., 2018; Capaldi et al., 2020; Mackaman-Lofland et al., 2020).

The Precordillera is separated from the Andean hinterland by the north-trending Iglesia-Calingasta-Uspallata basin (Beer et al., 1990; Podesta et al., 2022). The Western and Central Precordillera thrust belt accommodated the majority of the Andean retroarc shortening (up to 100 km E-W) via imbricate thrusting above a ~4–12 km deep décollement within Ordovician-Lower Devonian strata (Von Gosen, 1992; Allmendinger and Judge, 2014). To the north, Central Precordillera structures involve six east-verging faults and associated fault-propagation folds that deform Paleozoic and overlying Cenozoic foreland basin cover strata (Allmendinger et al., 1990; Jordan et al., 1993). Stratigraphy in the Central Precordillera consists of Cambrian-Ordovician carbonates, siliciclastic, and sedimentary mélange deposits that are unconformably covered by Silurian-Devonian marine rocks (Von Gosen, 1992; Keller, 1999; Mardonez et al., 2020). Structural and sedimentologic analyses of basin deposits found within the Central Precordillera as well as Bermejo foreland basin deposits indicate deformation and erosion initiated around 18-16 Ma, with a major phase of shortening-induced exhumation at 12-9 Ma (Beer and Jordan, 1989; Jordan et al., 1990, 1993; Allmendinger and Judge, 2014; Levina et al., 2014; Fosdick et al., 2015; Suriano et al., 2017; Mackaman-Lofland et al., 2022).

The Eastern Precordillera is a nearly 400 km long thrust front along the western Bermejo foreland basin. Cambrian-Ordovician carbonate rocks exposed in the Eastern Precordillera comprise the sedimentary cover overlying Cuyania basement. Previous work in the northern Eastern Precordillera (~30°S) identified the controlling structure as a hybrid thin- and thick-skinned triangle zone, where the Central Precordillera represents an east-verging, thin-skinned thrust system and the Eastern Precordillera represents a west-verging basement-involved thrust kinematically linked to the Sierras Pampeanas (Zapata and Allmendinger, 1996; Mardonez et al., 2020). The west-verging thrusts of the southern Eastern Precordillera (at the latitudes of the Rio San Juan ~31.5ºS) have been interpreted as a back-thrust zone to the Argentine Precordillera, possibly in response to the reactivation of older reverse faults (Von Gosen, 1992; Meigs et al., 2006).

The Bermejo foreland basin is structurally partitioned by the Sierras Pampeanas, which define predominately variably-orientated ranges uplifted along moderately to steeply dipping basement-involved thrusts (González Bonorino, 1950; Ramos et al., 2002). The western Sierras Pampeanas include the Sierra Valle de Fértil and Sierra Pie de Palo, which thrust Precambrian-Ordovician igneous and metamorphic rocks over Neogene foreland basin deposits (Fig. 2; Ortiz et al., 2015, 2021). The Mesoproterozoic basement assemblages exposed throughout the Sierras Pampeanas record polyphase deformation attributed to Pampean (555-515 Ma) and Famatinian (495-460 Ma) orogenesis during accretion of Laurentian terranes to the Gondwanan margin (Casquet et al., 2001; Ramos, 2004; Mulcahy et al., 2011, 2014; Tholt et al., 2021). Low temperature thermochronology and stratigraphic constraints from the western Sierras Pampeanas ranges record Andean deformation around 5 Ma (Ortiz et al., 2015, 2021; Capaldi et al., 2020). The presence of older, Permian-Cretaceous cooling ages has been attributed to protracted cooling over the past 20 Myr, or the existence of topographic relief prior to reverse faulting during the Andean Orogeny (Ortiz et al., 2015, 2021; Stevens-Goddard et al., 2018). The Eastern Precordillera and Sierras

Pampeanas domains remain active today, as evident from high seismic activity in the surrounding regions that has resulted in the most devastating earthquakes in Argentine history (Siame et al., 2002; Alvarado and Beck, 2006; Meigs et al., 2006; Vergés et al., 2007; Rimando and Schoenbohm, 2020; Venerdini et al., 2020).

The Bermejo foreland basin lies between the Precordillera fold-thrust belt and Sierras Pampeanas and can be divided into the northern Bermejo basin, which lies north of 31°S and includes the previously studied Huaco (Johnson et al., 1986; Jordan et al., 2001; Fosdick et al., 2015) and Mogna (Milana et al., 2003; Capaldi et al., 2020) localities, and the southern Bermejo basin within the Tulum Valley is situated south of 31°S and includes the Ullum (Bercowski et al., 1987; Contreras et al., 2019) and Villicum localities, which are the focus of this work (Fig. 2). Between the northern and southern Bermejo basin localities lies the east-west trending North Pie de Palo fault, which delineates the northern tip point of lower Paleozoic strata of Sierra Villicum and the contact between metamorphic rocks of Sierra Pie de Palo and Neogene and Quaternary deposits (Fig. 2; Zapata, 1998; Siame et al., 2015). Based on cross-cutting relationships and geochronologic data from Sierra Pie de Palo, the North Pie de Palo fault most likely developed during the Ordovician-Silurian Famatinian orogeny during the accretion of the Cuyania terrane, which includes the Eastern Precordillera and Sierra Pie de Palo, with the Gondwanan margin (Vujovich et al., 2004; Mulcahy et al., 2011). This lineament coincides with northward deepening of the depth to basement, from ~2 km in the south to >7 km in the north (Jordan and Allmendinger, 1986), as well as a northward decrease in seismicity (Smalley et al., 1993; Venerdini et al., 2020). Preexisting structural and stratigraphic anisotropies have been shown to affect foreland subsidence patterns, basin geometry, and stratigraphic stacking patterns in Andean retroarc basin settings (Kley et al., 1999; Fosdick et al., 2014; McGroder et al., 2015; Horton et al., 2022b).

3. Sedimentology

This study focuses on two new stratigraphic sections in the southern Bermejo basin at the Villicum and Ullum localities, with an emphasis on correlation with northern Bermejo sections (Fig. 3). The Villicum section was measured utilizing three-to 5-m-high outcrops exposed within

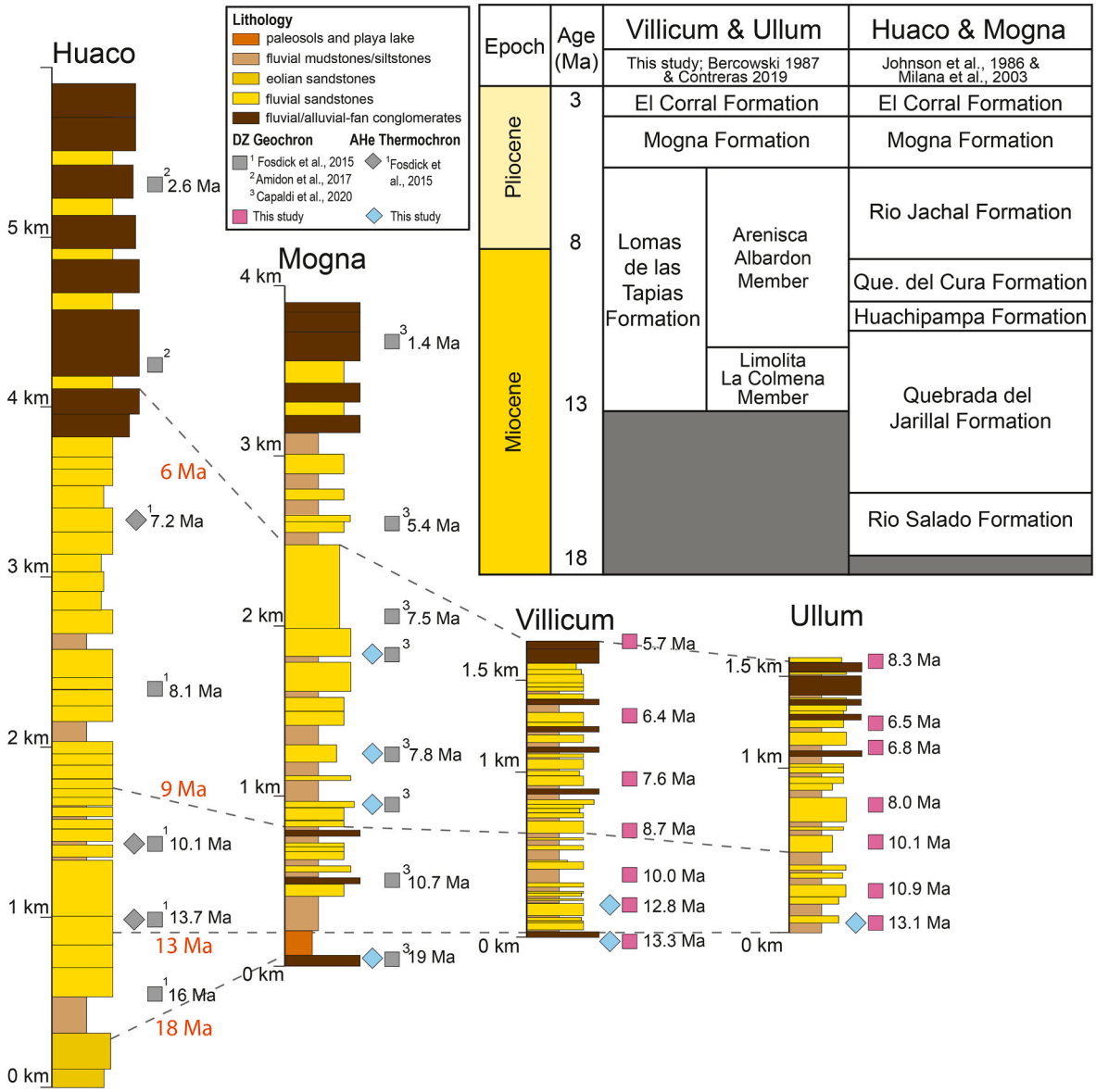

Fig. 3. Schematic Miocene to Pliocene stratigraphic sections with associated maximum depositional ages, and correlated timelines across the Argentina retroarc broken foreland basin system. The Huaco and Mogna sections were redrafted from Johnson et al. (1986) and Milana et al. (2003), respectively. Sample location of detrital zircon U–Pb geochronology (squares) and apatite (U–Th-Sm)/He thermochronology (diamonds).

small, incised stream channels east of the Eastern Precordillera (Fig. 2). The Ullum section was measured along well-exposed outcrops along the Río San Juan northeast of the city of San Juan (Fig. 2). Exposure and land accessibility became difficult near the top of the measured sections, and therefore the stratigraphic thicknesses presented do not represent the full thickness of basin deposits. The estimated total thickness of each stratigraphic section is ~1800 m.

New sedimentological constraints from the Villicum and Ullum localities are expected to reveal changes in foreland depositional environments, sediment provenance, and accumulation rates as the retroarc region was structurally partitioned by Andean ranges. Southern Bermejo stratigraphic sections consist of the Miocene Lomas de las Tapias Formation comprised of the Limolita la Colmena and Arenisca Albardón Members, the Mogna Formation, and the El Corral Formation (Fig. 3; Bercowski et al., 1987; Contreras et al., 2019). The Limolita la Colmena Member correlates with the upper Quebrada del Jarillal Formation, and the Arenisca Albardón Member correlates with the Huachipampa, Quebrada del Cura, and Rio Jachal Formations of the northern Bermejo basin (Fig. 3; after Johnson et al., 1986; Milana et al., 2003).

To assess depositional processes and environments, lithological descriptions, bed thicknesses, facies, and sedimentary structures were described at the decimeter scale in the field. Lithofacies are modified after Miall (1977) and are presented in Table 1 along with depositional environment interpretations. Paleoflow directions were determined from imbricated conglomerate clasts (n = 15) from localities within the Ullum and Villicum sections (Supplemental File 1). Imbricated conglomerate clast measurements were then corrected for bedding dip using the Stereonet 11 program (Allmendinger et al., 2012). Mean azimuthal vectors were calculated using the GeoRose software and plotted as paleoflow direction at corresponding stratigraphic heights.

Pebble to boulder sized conglomerate clast compositional data were collected from eight locations within the Villicum section and nine locations within the Ullum section (Fig. 4; Tables 2 and 3; Supplemental File 2). At each clast count site, 100+ clasts were identified within a 1 m^2 area according to procedures outlined by Howard (1993). Clasts were divided into seven categories: (1) intermediate to felsic volcanic rocks consisting of maroon, brown, and red andesite, dacite, and rhyolite volcanic rocks and gray volcaniclastics; (2) felsic intrusive rocks consisting of granitic to granodiorite compositions; (3) mafic to intermediate volcanics consisting of green to gray andesites and black phenocrystic basalts; (4) meta-sedimentary rocks consisting of green to tan metamorphosed sandstone and siltstone; (5) brown, gray, and red silt- and sandstones; (6) metamorphic lithologies including amphibolite gneiss, schist, marble, and vein quartz; and (7) black chert, blue-gray limestone, and dolostone.

3.1. *Miocene Lomas de las Tapias Formation: Limolita la Colmena Member*

The approximately 325-m-thick Limolita la Colmena Member of the Lomas de las Tapias Formation overlies an angular unconformity with the underlying Cambrian La Lajas Formation at Ullum and the Silurian Rinconada Formation at Villicum (Fig. 2). The Limolita la Colmena member largely consists of <5–~20 m of thickly-bedded mud-to siltstones (*Fr;* Facies 1) and thin <1 m to up to ~5 m thick interbedded very fine to medium grained sandstones (*Fl;* Facies 2) that are more commonly found near the top of the member. There are several occurrences of ~1-m-thick granule-pebble conglomerate units within the member which provide the opportunity for paleoflow measurements and conglomerate clast counting. The Limolita la Colmena Member is generally an upward-coarsening sequence with facies both coarsening and thickening up-section. Within the Limolita la Colmena Member, abundant gypsum and carbonate nodules (<5 cm in diameter*; P)*, are observed within the mudstone-siltstone units. At the Villicum section, gypsum is also present in vast vein networks (~1–5 cm) spanning entire mudstone beds of ~3–5 m in thickness (Fig. 5a). The member is heavily mottled, displaying irregular coloration with frequent occurrences of bioturbation and root structures throughout, and minor occurrences of desiccation structures (*Fr, Fm*; Fig. 5b and c). In Villicum, the Limolita la Colmena member also displays mud rip-up clasts, which was not noted

Table 1
Facies association and interpretations for southern Bermejo basin deposits.

Facies association	Lithofacies	Description	Occurrence	Interpretation
1	Fr, P	Massive reddish mud-siltstones. Mottled, bioturbated, common carbonate and gypsum modules/ veining	Limolita la Colmena Mbr.	Playa lake, paleosol
2	Fl, Fr, Fm, Fsm	Massive red-tan mud-siltstones grade into very fine to medium grained sandstones that are laterally continuous. Bioturbation and desiccation crack features common.	Limolita la Colmena Mbr.; Arenisca Albardón Mbr.; Mogna Fm.	Floodplain
3	Sr, Sl, St, Sh, Fm	Very-fine to fine grained sandstones interbedded with mudstones. Tabular sheet like bodies. Upward thickening and coarsening packages. Desiccation cracks and mudstone intraclast in sandstone base.	Arenisca Albardón Mbr.; Mogna Fm.	Crevasse splays
4	Sl, St, Sp, Gp, Gh, Gt	Amalgamated medium to very coarse cross-bedded and laminated sandstones. Upward fining Laterally continuous with flat channel bottoms. Interbedded cross-bedded and imbricated granule-pebble conglomerates.	Arenisca Albardón Mbr.; Mogna Fm.	Low-sinuosity braided sand and gravel fluvial channels
5	Gh, Gp, Sr, Ss, Sl	Moderately sorted granule-cobble clast supported conglomerates. Finning upward sequences to silt-sandstones. Tabular amalgamated channel bodies.	Mogna Fm.	Large braided gravel fluvial channels
6	Gmm, Gmg, Gcm, Sm	Brown matrix to clast supported, poorly sorted, cobble to boulder conglomerate. Interbedded lenticular sandstones.	El Corral Fm.	Debris flow deposits on alluvial fan

at Ullum. Sandstones within the member are laterally continuous and display minor ripple structures and fine (cm-scale) planar lamination (*Sl*).

Paleocurrent data collected on imbricated clasts in the Limolita la Colmena Member show a south-southeast trend from measurements collected in Ullum and a southeast trend from Villicum (Fig. 4). Conglomerate clast composition of the Limolita la Colmena Member in the Ullum section is dominated by felsic volcanic rocks (47%), metasedimentary rocks (27%), and mafic volcanics (19%). The remaining 9% of clasts consist of minor portions of felsic intrusive rocks and crystalline

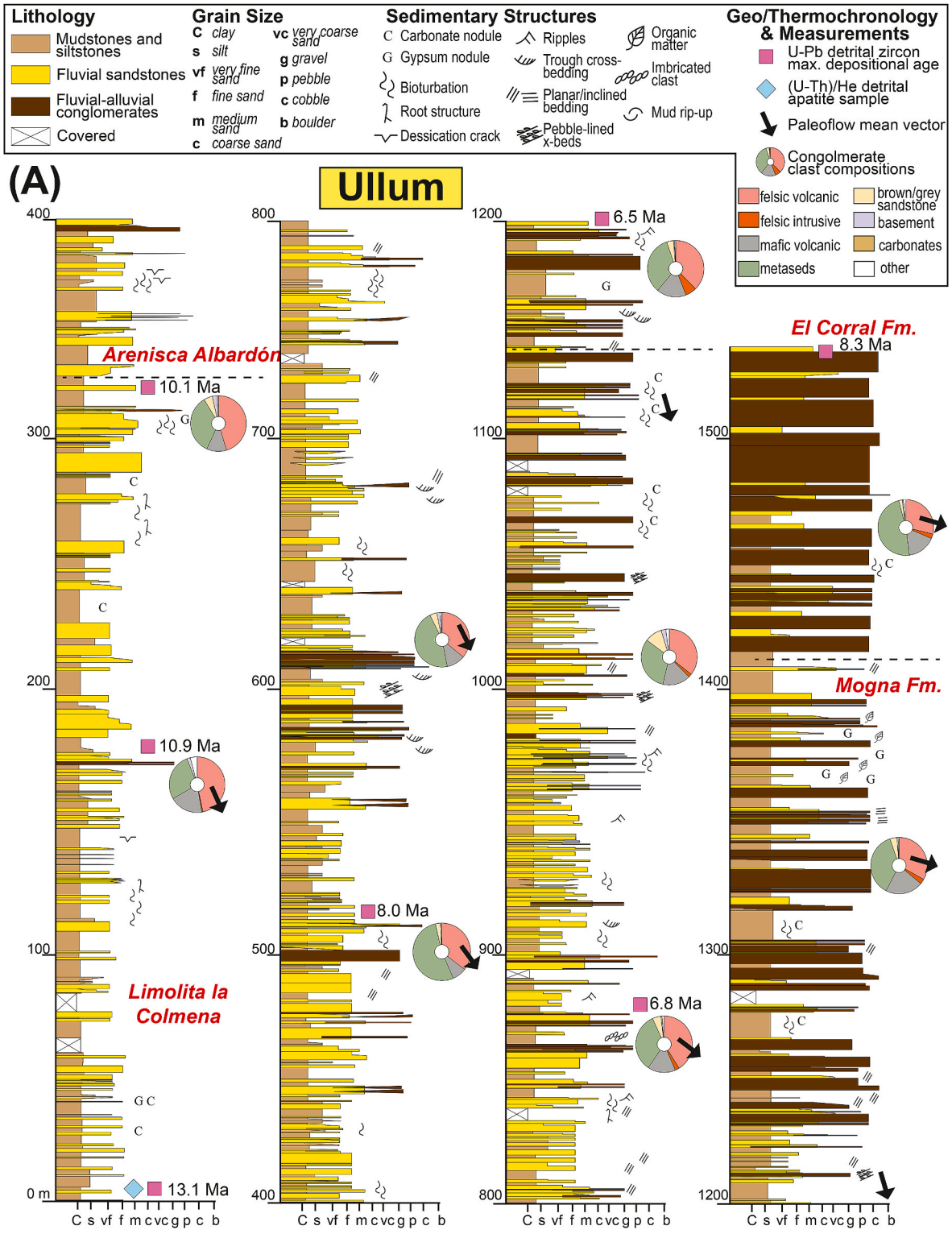

Fig. 4. A) Stratigraphic section from the Ullum locality in the southern Bermejo basin. Section shows locations of rock samples and associated depositional age, paleocurrent measurements (arrows), clast count compositions (ring diagrams), and observed sedimentary structures.
Fig. 4 (continued). B) Stratigraphic section from Villicum locality in the southern Bermejo basin. Sections show location of rock samples and associated depositional age, paleocurrent measurements (arrows), clast count compositions (ring diagrams), and observed sedimentary structures.

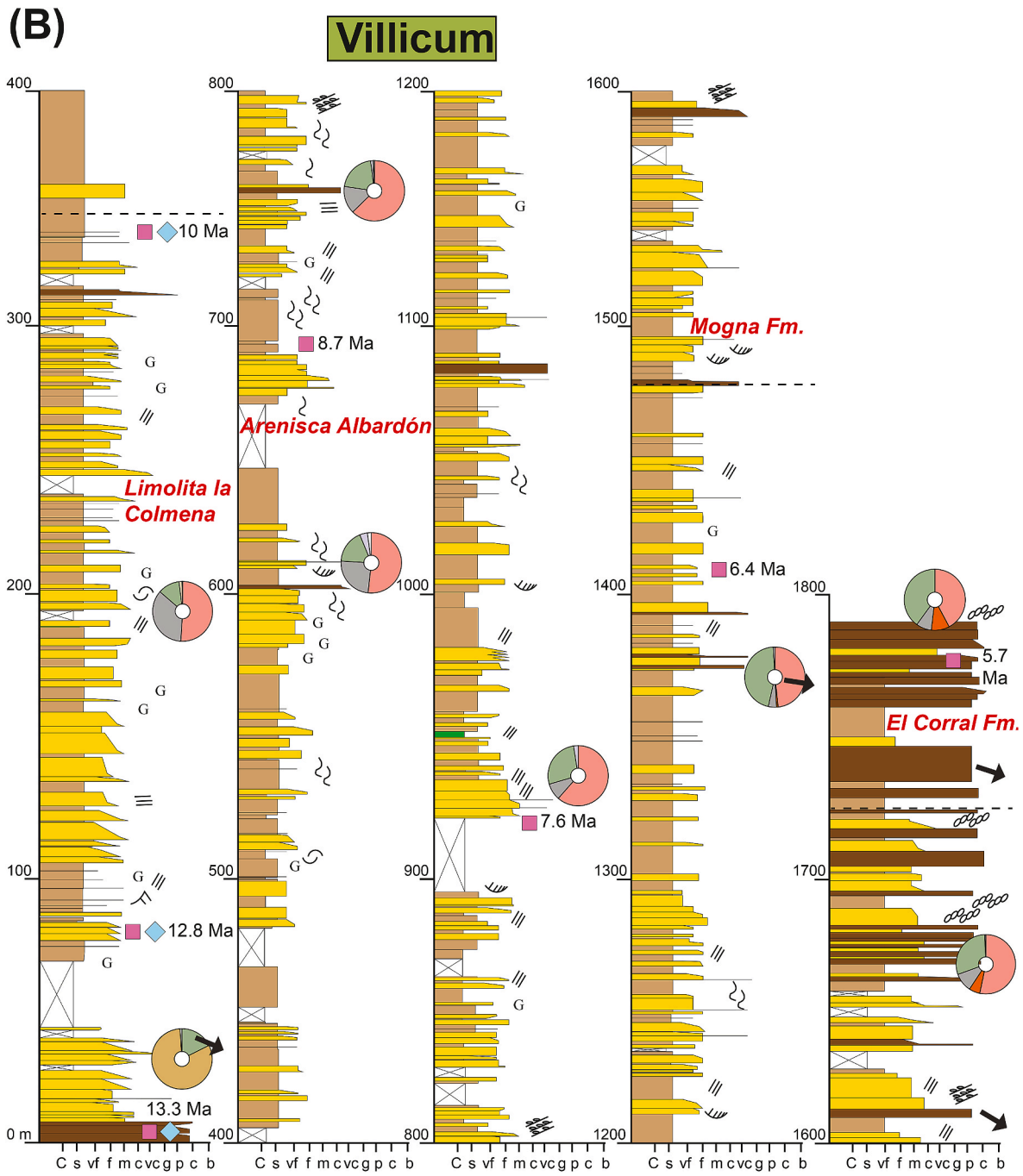

Fig. 4. (*continued*).

basement rock lithologies. In the Villicum section, the base of the Limolita la Colmena member shows input of Paleozoic carbonate lithologies, representing 81% of clast composition. The remaining 19% consists of metasedimentary clasts. In the upper part of the member, the Villicum section displays similar trends to Ullum with the dominating lithologies being: felsic volcanics (50%), mafic volcanics (~30%), and metasedimentary rocks (~15%).

The Limolita la Colmena Member has previously been interpreted to represent a playa lake depositional environment (Bercowski et al., 1987; Contreras et al., 2019). The observed upward coarsening sequence, with massive reddish muds that grade into thicker sand channels could further indicate a flood-plain environment (Limarino et al., 2001). Additionally, there are distinct fluvial signals within the Limolita la Colmena Member, represented by the upward thickening packages of laterally continuous sandstones which may indicate unconfined flow in a floodplain, e.g., crevasse splay facies (Horton and DeCelles, 2001). The observed stratigraphic trend of playa lake/paleosol mud-siltstones overlain by fluvial sandstone channels may suggest avulsion of channels within this distal floodplain environment (DeCelles et al., 1998; Horton and DeCelles, 2001). The presence of playa lake-floodplain facies with a distinct fluvial signature may be indicative of a developing fluvial megafan sequence in which the Limolita la Colmena member represents the furthest reaches of an eastward migrating system (e.g., Horton and DeCelles, 2001; Lawton et al., 2014).

3.2. Miocene Lomas de las Tapias Formation: Arenisca Albardón Member

Arenisca Albardón, the uppermost member of the Lomas las Tapias

Formation, conformably overlies the Limolita la Colmena Member, and is ~775 and ~1050 m thick at Ullum and Villicum, respectively. Arenisca Albardón contains packages of bioturbated and occasionally desiccated mudstones and siltstones (*Fr, Fm;* Fig. 5c) overlain by laminated and diffusely rippled fine to coarse grained sandstones (*Sl, Sr*). The mudstones and siltstones rarely contain gypsum/carbonate nodules. Recurring mudstone-sandstone sequences range from 0.25 to 5 m thick (facies 3). Also significant in the Arenisca Albardón Member are frequent very fine to very coarse sand bodies which display trough and planar cross bedding *(St, Sp;* Fig. 5g) and planar laminae (*Fl*) (facies 4). These sand bodies typically outcrop as multi-story sandstone beds and display flat channel bottoms that are laterally continuous. Granule to pebble clasts are locally present within sandstone beds as floating clasts and occasionally define cross stratification (Fig. 5g). Within this sequence there are significant amount of granule-pebble conglomerate beds which display planar-trough cross stratification and imbricated clasts *(Gp, Gt, Gh)*. Conglomerate beds are typically interbedded within the sandstone bodies of facies 4 or within upward fining sequences where thin conglomerate beds are overlain by the sandstone and siltstone units of facies 3 (<5-m packages). The Arenisca Albardón Member is composed of repeated fining upward sequences of mudstone, siltstone, and sandstone packages (facies 3) and laterally continuous cross-bedded sand bodies with interbedded conglomerate beds (facies 4) on scales ranging from 5 up to 50 m thick (Fig. 5d and h).

Paleocurrent measurements from imbricated conglomerate clasts in the Arenisca Albardón Member record south-southeast paleoflow from Ullum sites and eastward paleoflow from Villicum sites (Fig. 4). Conglomerate clast compositions in the Ullum section record a notable decrease in the input of felsic volcanic rocks, from 45% at the base to 36% at the top of the member. The percent composition of metasedimentary clasts increases up-section, reaching a maximum of 53% at 525 m and then steadily declining to 32% at the top of the Arenisca Albardón Member. Mafic volcanic clasts drop to a minimum of 8% at 525 m (synchronous with maximum metasedimentary input) then stabilize to around 16% near the top of the member. Within the Villicum section, felsic volcanic clasts initially increase from 52% to 63% near the lower to middle member and then decrease to 48% at the top. At this location, metasedimentary clasts steadily increase to 46%, becoming more dominant than mafic volcanics, which decrease to <5% at the top of Arenisca Albardón deposition. Both section locations display low abundances (<10%) of felsic intrusive, brown-red-tan silt-sandstones, and basement rock clasts.

Relative to the Limolita La Colmena Member, the Arenisca Albardón Member represents an increasingly more fluvial environment where the dominant thick, cross-bedded sandstones signify deposition in broad braided river channels and the bioturbated, mottled mud-silt-sandstones represent overbank deposition of finer grained sediment (Miall, 1977; Ciccioli et al., 2018). The laterally continuous flat channel bottoms noted consistently in the multi-story sandstone beds (facies 4) imply no significant incision into adjacent floodplain deposits, indicative of

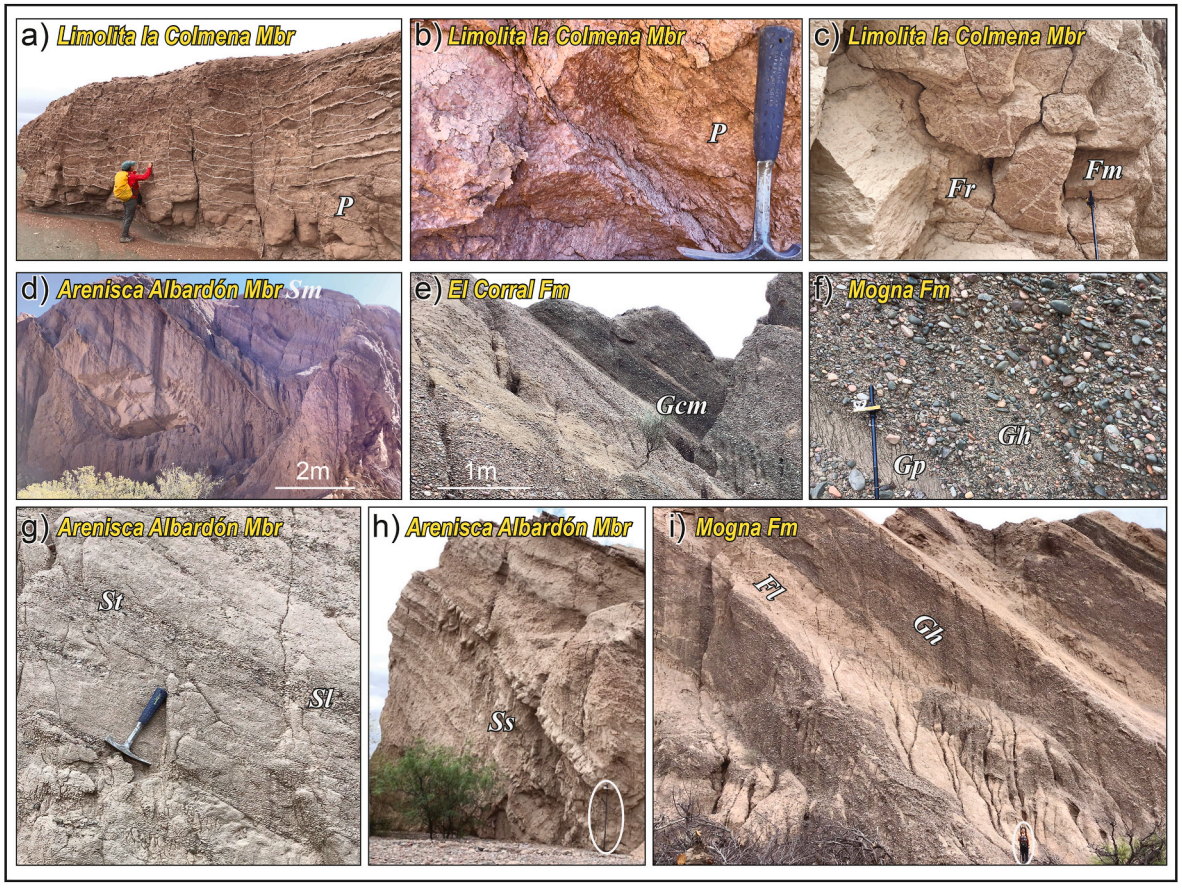

Fig. 5. Field photographs of sedimentary deposits of the Villicum and Ullum sections. (A) Gypsum veins (P) in the Limolita la Colmena Member at Villicum. (B) Limolita la Colmena paleosol facies at Ullum (P); mottled mudstone-siltstone displaying discoloration and bioturbation. (C) Desiccation structures preserved in mud-siltstone (Fm) with roots and bioturbation (Fr) in Limolita la Colmena at Ullum. (D) Large-scale packages of laterally continuous, flat bottomed sandstone beds (Sm) diagnostic of the Arenisca Albardon Member at Ullum (30-50-m packages). (E) Poorly sorted, structureless cobble-dominated conglomerate (Gcm) of the El Corral Formation at Ullum. (F) Imbricated and weakly cross-bedded pebble conglomerates (Gp, Gh) of the Mogna Formation at Ullum. (G) Cross-bedded sandstone (St, Sl) of the Arenisca Albardon Member at Ullum incorporating coarser-grained sediment, at Ullum. (H) Crevasse splay facies of the Arenisca Albardon Member at Ullum (~5-10-m packages). Jacob staff for scale in white outline. (I) Interbedded pebble-cobble conglomerates (Gh) and silt-sandstone (Fl) of the Mogna Formation at Ullum. Person for scale in white outline.

channel avulsion rather than migration (Horton and DeCelles, 2001). Further, the preservation of thick sandy (flat-bottomed) channels interbedded with overbank facies consistently repeated throughout the Arenisca Albardón Member suggests a lack of channel stability over time and is typical of ancient fluvial megafan sequences (Horton and DeCelles, 2001).

3.3. Pliocene Mogna Formation

The Pliocene Mogna Formation conformably overlies the Lomas de las Tapias Formation and is ~300–325 m thick in southern Bermejo basin. The Mogna Formation largely consists of pebble to cobble conglomerates (facies 5) that are moderately-sorted, contain rounded to well-rounded clasts and are typically clast-supported (*Gh*). Conglomerate beds also contain imbricated clasts and planar cross-stratified beds (*Gp, Gh*; Fig. 5f). Thin beds of siltstone to very coarse sandstones typically overly the more abundant conglomerate facies and define upward fining sequences ranging from 2 to 20 m thick (Fig. 5i). Siltstones display minor bioturbation (*Fr*) and sandstone beds show minor trough-cross to inclined bedding and occasionally preserve meter scale scour and fill structures infilled by conglomerates (*Ss, Sl*). Sandstone-pebble conglomerate channel bodies most commonly preserve planar bases.

Paleoflow data from the Mogna Formation collected on imbricated conglomerate clasts from southern Bermejo basin records south-southeast to southeast sediment dispersal. Within the Mogna Formation at Ullum, felsic volcanic rocks remain a steady contributor of conglomerate clasts at ~35% and mafic volcanic clasts reach a maximum in the upper Mogna Formation at 22%. Metasedimentary clast input increases slightly relative to the underlying member to 37%, while brown-red-gray silt-sandstones decrease from their maximum at the top of Arenisca Albardón deposition to 4%. In the Villicum section, felsic and mafic volcanics increase slightly, to 53% and 10% respectively. Metasedimentary contribution decreases to 30% and the remaining categories (felsic intrusive and basement lithologies) remain at <10% composition.

The Mogna Formation is interpreted to represent a gravel-dominated braided fluvial environment based on observations of internally upward fining cycles of conglomerate and coarse sandstone capped by silty mudstones (Miall, 1977, 1985; Ciccioli et al., 2018; Capaldi et al., 2020). This broad braided river is interpreted to represent the main channel of the fluvial megafan system that was continuing to migrate eastward at this time due to deformation in the hinterland, based on observations of planar channel bases and continued preservation of overbank facies (Horton and DeCelles, 2001). Upward coarsening successions, as seen in both Villicum and Ullum, where ephemeral lake systems grade into sandy to coarse conglomerate avulsing channel deposits with interbedded overbank/crevasse splay facies, record progradation of a fluvial megafan (Horton and DeCelles, 2001; Lawton et al., 2014).

3.4. Pliocene El Corral Formation

The Pliocene El Corral Formation rests conformably on the Mogna Formation and was locally measured to 60 and 125 m thick at Villicum and Ullum, respectively. Estimates of total thickness made from the measured dip of stratigraphy and distance to the top of section determined via satellite imagery indicates that the El Corral Formation deposits may be up to 300 m thick. The El Corral Formation is dominated by pebble to cobble conglomerate lithofacies with occasional floating boulder-sized clasts, and is matrix to clast supported, poorly sorted, and structureless (*Gcm;* Fig. 5e). The conglomerate units are interbedded with thin (0.5 to <5 m) beds of medium to coarse grained sandstone near the base and grade into siltstone up-section (*Fl-Sm*), defining internally upward fining packages from 5 to 20 m thick.

Paleocurrent data collected on imbricated clasts at both southern Bermejo localities from the El Corral Formation indicate east-southeast to southeast paleoflow directions. Conglomerates of the El Corral Formation in Ullum are dominated by metasedimentary clasts (48%). Felsic volcanic rock input remains steady at ~30% and mafic volcanic clasts decreased relative to the underlying member, reaching the section average of ~16%. Felsic intrusive rocks, brown-gray-red silt-sandstones, and basement rocks individually contribute <5%. In Villicum, the El Corral Formation is similar to that described at the Ullum location, with 42% felsic volcanic input and 40% metasedimentary rock input. Felsic intrusive rock clasts reach a maximum of 10% while mafic volcanics remain steady around ~8%.

The poorly sorted, structureless pebble-cobble conglomerate facies of the El Corral Formation are interpreted as gravelly debris flows and late-stage sandy hyperconcentrated flows on an alluvial fan (Nemec and Steel, 1984; Horton and Schmitt, 1996; Perez and Horton, 2014). The El Corral debris flow deposits are interbedded with fluvial silt and sandstone units (such as the braided river channels observed in the Arenisca Albardón Member) and likely signal an increase in sediment transport energy associated with the encroaching Precordillera topographic and thrust front toward the foreland (Jordan et al., 1993; Capaldi et al., 2020).

4. Detrital Zircon U–Pb Geochronology

We collected 14 sandstone samples within the measured stratigraphic sections (Fig. 4) and an additional 2 sandstone samples (ULL01 and VIL01) not in the stratigraphic sections (Fig. 2; Appendix E). We targeted medium-grained sandstones for zircon U–Pb geochronology to determine maximum depositional ages of Neogene units and to constrain changes in sediment provenance during uplift and erosion of Andean ranges. Zircon is a highly refractory mineral that incorporates high concentrations of U combined with low amounts of initial Pb, providing precise age controls for the crystallization of intermediate to felsic igneous rocks and high-grade metamorphic rocks (Gehrels, 2014; Rubatto, 2017).

4.1. Analytical Methods and Data Visualization

Zircons were extracted from sandstones using standard separation procedures including crushing, grinding, water table, heavy liquid density, and magnetic susceptibility. Zircon grains were handpicked using an optical microscope, targeting non-broken, inclusion-free grains, and were mounted on double sided tape on 2.5 cm diameter epoxy resin mounts. Zircon grains were chosen randomly for analysis by laser-ablation-inductively coupled plasma-mass spectrometry (LA-ICP-MS) to obtain zircon U–Pb ages.

Sandstone samples from the Villicum section and basal Ullum sample ULL01 were analyzed for detrital zircon geochronology at the University of Texas at Austin UTChron laboratory. Zircon sample mounts were loaded into a large-volume Helex sample cell and ablated using a PhotonMachine Analyte G.2 excimer laser for analysis with a single-collector, magnetic sector Element2 ICP-MS (for more details see Capaldi et al., 2021). Corrections for depth dependent, elemental and isotopic fractionation were performed using zircon standard GJ1 (600.4 ± 0.1 Ma; Jackson et al., 2004). Secondary standards were analyzed periodically to verify the accuracy of the analyses; these included the Plesovice zircon (PL-1; 337.2 ± 0.4 Ma; Sláma et al., 2008) and Pak-1 (43.03 Ma; in-house standard).

Sandstone samples from the Ullum section were analyzed for detrital zircon geochronology at the University of Nevada, Las Vegas Nevada Plasma Facility Lab. Zircon sample mounts were loaded into a TwoVol 1 ablation cell and ablated using an ESI 193 nm NWR193 excimer laser for analysis with a Quadruple collector ThermoFisher Scientific TM iCAP ICP-MS (for more details see Garzanti et al., 2022). Corrections for depth-dependent, elemental and isotopic fractionation were performed using zircon standards FC1 (1099 ± 0.5 Ma; Paces and Miller, 1993) and secondary standards Plesovice (PL-1; 337.2 ± 0.4 Ma; Sláma et al., 2008) and Fish Canyon Tuff (28.4 ± 0.02 Ma; Schmitz and Bowring,

2001).

Zircon analyses from both labs were reduced using the VizualAge™ workflow in the Iolite™ plugin for Igor Pro™ (Paton et al., 2011; Petrus and Kamber, 2012). Zircon U–Pb ages and 2σ errors are reported for analyses with <10% $^{206}Pb/^{238}U$ uncertainties, <20% discordance, and <5% reverse discordance. Reported values for grains <1200 Ma are $^{206}Pb/^{238}U$ ages with $^{206}Pb/^{238}U$ vs. $^{207}Pb/^{235}U$ discordance, whereas values for grains >1200 Ma ages are $^{207}Pb/^{206}Pb$ ages with $^{206}Pb/^{238}U$ vs. $^{207}Pb/^{206}Pb$ discordance. Miocene zircons (<23 Ma) were expanded to incorporate ages with <20% $^{206}Pb/^{238}U$ uncertainties and <50% discordance $^{206}Pb/^{238}U$ to prevent biasing due to exclusion of young grains with higher ^{207}Pb and associated $^{207}Pb/^{235}U$ ages that are systematically older than the measured $^{206}Pb/^{238}U$ ages. Detrital zircon geochronology data for samples analyzed at University of Texas at

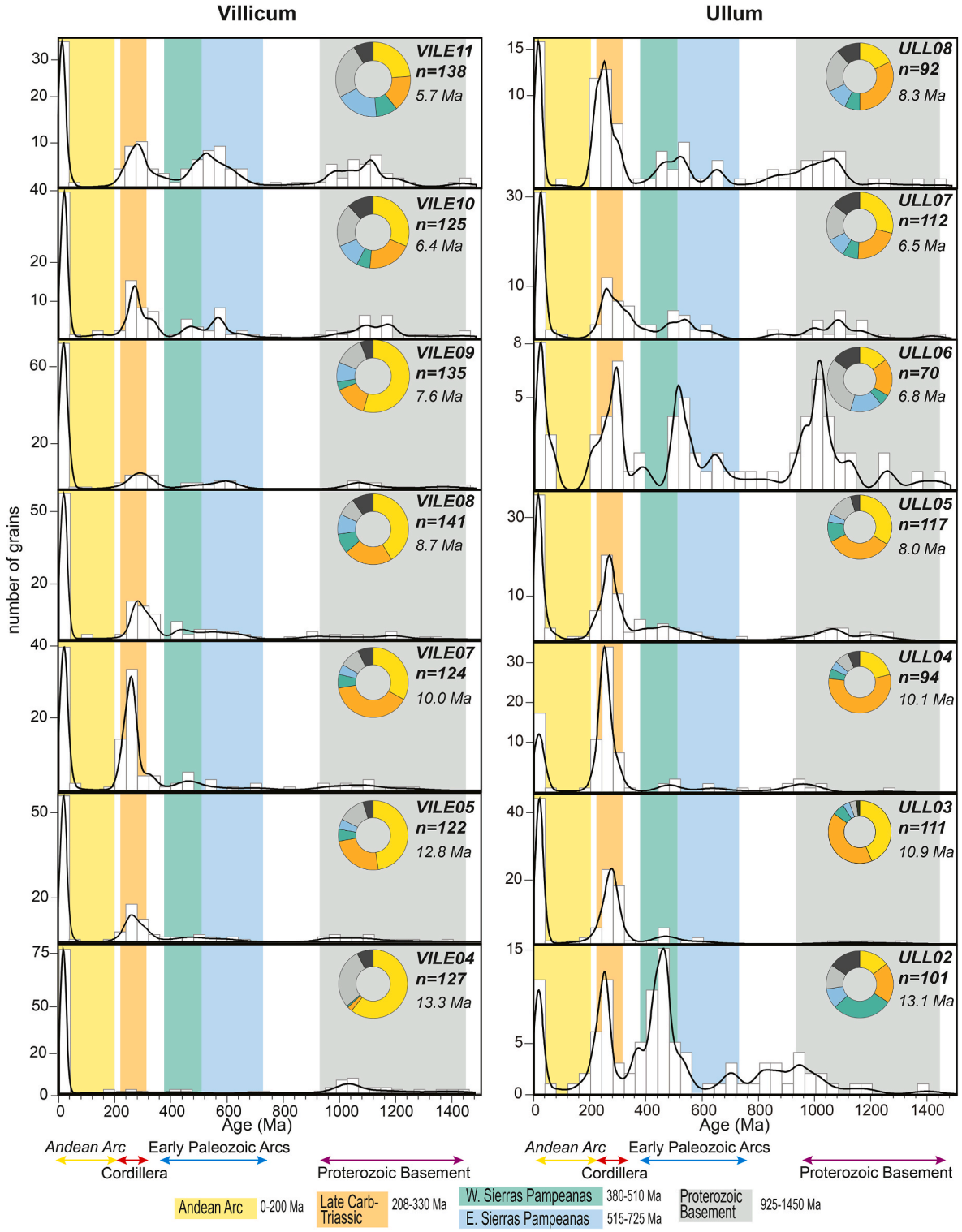

Fig. 6. Comparative plot of detrital zircon U–Pb age distributions for sandstone samples from the Villicum and Ullum sections. Distributions depicted as kernel density estimates (20 Myr bandwidth) and age histograms with emphasis on key age components (color shading). Ring diagrams at right present the relative abundance of key age components with color shading representing key age components with the addition of dark gray for "other" age components.

Austin UTChron lab can be found in Supplemental File 3 and data for samples analyzed at UNLV NPFL can be found in Supplemental File 4.

Results for individual samples are arranged in stratigraphic order and are represented as kernel density estimations (KDEs) with a set bandwidth of 20 Myr and histogram age bins with a 40 Myr bin width (Figs. 6–8) and were plotted using IsoplotR (Vermeesch, 2018). Comparison among sample U–Pb age distributions was accomplished by visual inspection of the relative abundance of age groups. Additional comparison of DZ-Ub age distributions was established through metric multidimensional scaling (MDS) plots to identify greater similarity for samples that cluster together and less similarity for those that plot farther apart. Metric squared MDS is applied by constructing a pairwise dissimilarity matrix of detrital age distributions among the sandstone samples using R^2 cross-correlation coefficient. The metric squared MDS plot and results were created using the program DZmds (Saylor et al., 2018). Detrital zircon samples from the Andean foreland deposits from the Ullum and Villicum sections were compared to each other and to previously published data from the Huaco section (Fosdick et al., 2015; Amidon et al., 2017) and Mogna section (Capaldi et al., 2020) using a three-dimensional (3D) MDS plot. The misfit from conversion of sample dissimilarity to disparity in Cartesian space via linear transformation provided a good correlation, as indicated by a low stress minimum (0.08).

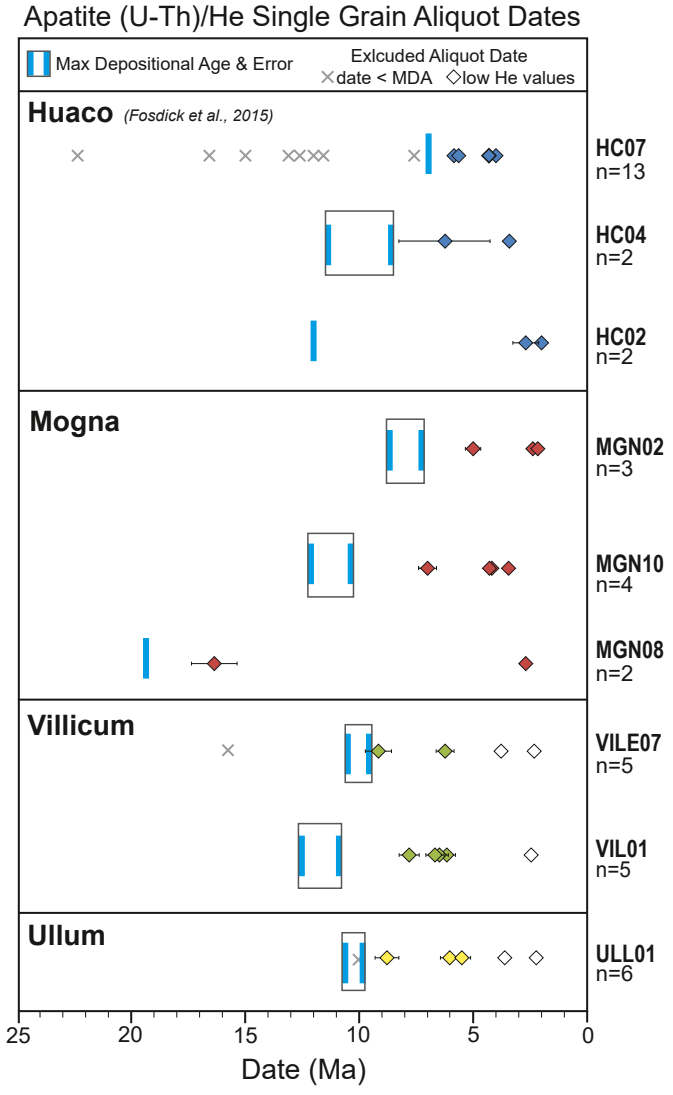

Fig. 7. Plot of apatite (U–Th-Sm)/He ages for new Mogna, Villicum, and Ullum samples, and published Huaco samples (Fosdick et al., 2015). All (U–Th-Sm)/He ages are plotted with 2σ error bars. For each locality, samples are presented in stratigraphic order, with maximum depositional ages denoted by boxes with blue bars as errors.

4.2. Maximum Depositional Ages

A maximum depositional age for the 16 sandstone samples was derived from the calculated weighted mean age of the youngest grain cluster overlapping by 2σ concordant U–Pb ages (following approaches established by Dickinson and Gehrels, 2009; Coutts et al., 2019). In cases where two or more grains do not overlap by 2σ, the youngest single grain was selected as the maximum depositional age (Supplemental File 5) and plotted at the corresponding stratigraphic level (Fig. 4).

Most Cenozoic sandstone samples contain young age populations broadly consistent with previous age assessments (Milana et al., 2003; Capaldi et al., 2020). Collectively, samples from the retroarc basin system show a systematic up-section decrease in maximum depositional age, with the exception of sample ULL08 (8.3 ± 0.1 Ma) from El Corral Formation in the Ullum section (Fig. 4). On the basis of the internal consistency and stratigraphic coherence, the calculated maximum depositional ages are regarded as viable approximations of stratigraphic age and we acknowledge the caveat that these are not true depositional ages.

4.3. Detrital Zircon Age Components

Here we describe five diagnostic age groups representative of sediment provenance signatures recorded by detrital zircon U–Pb analyses from oldest to youngest.

1. Proterozoic zircon ages (~925–1450 Ma) ages include a 1350–1450 Ma age component recycled from Cambrian-Ordovician strata and unique to the Cambrian-Orodovcian strata of the Eastern Precordillera (Ramos et al., 1986; Thomas et al., 2015; Martin et al., 2019). Dominant 925–1200 Ma zircon age components may have been sourced from numerous Sunsas metamorphic basement units that presently outcrop across the Sierra Pie de Palo and are ubiquitous in most Ordovician to Permian sedimentary sequences deformed within the central Precordillera (Ramos, 2004, 2009; Bahlburg et al., 2009; Rapela et al., 2016).
2. The Eastern Sierras Pampeanas (515–725 Ma) age group is composed of a minor 725-550 Ma age component initially recycled from metasedimentary rocks (Puncoviscana Formation) and a dominant 515–550 Ma age peak originally from igneous-metamorphic rocks of the Pampean magmatic arc presently exposed in Sierra Cordoba (Schwartz et al., 2008; Rapela et al., 2016). The Eastern Sierras Pampeanas (515–725 Ma) age group zircons are commonly recycled from Carboniferous to Permian sedimentary sequences found in the central Precordillera fold-thrust belt (Fosdick et al., 2015; Capaldi et al., 2017, 2020).
3. The Western Sierras Pampeanas (380–510 Ma) age group is derived from sources throughout the western Sierras Pampeanas involving 440–505 Ma Famatinian continental arc rocks in the Sierra Valle Fertíl (Ducea et al., 2010; Otamendi et al., 2017; Rapela et al., 2018) and subsequent 385–435 Ma metamorphic assemblages associated with accretion of the Cuyania terrane (Coira et al., 1982; Martin et al., 2019). Recycled western Sierras Pampeanas 380–510 Ma DZ age components are derived from Carboniferous-Permian sedimentary units in the Precordillera fold-thrust belt and Carboniferous-Triassic sedimentary sequences overlying western Sierras Pampeanas uplifts (Capaldi et al., 2017).
4. Late Carboniferous-Triassic zircon ages (225–330 Ma) are derived from intrusive and volcanic rock sources throughout the Chilean Coastal Cordillera, Frontal Cordillera, and Principal Cordillera. These rocks include the 290–310 Ma Elqui-Limari and the Colangüil batholiths (Maksaev et al., 2014; Hervé et al., 2014; del Rey et al.,

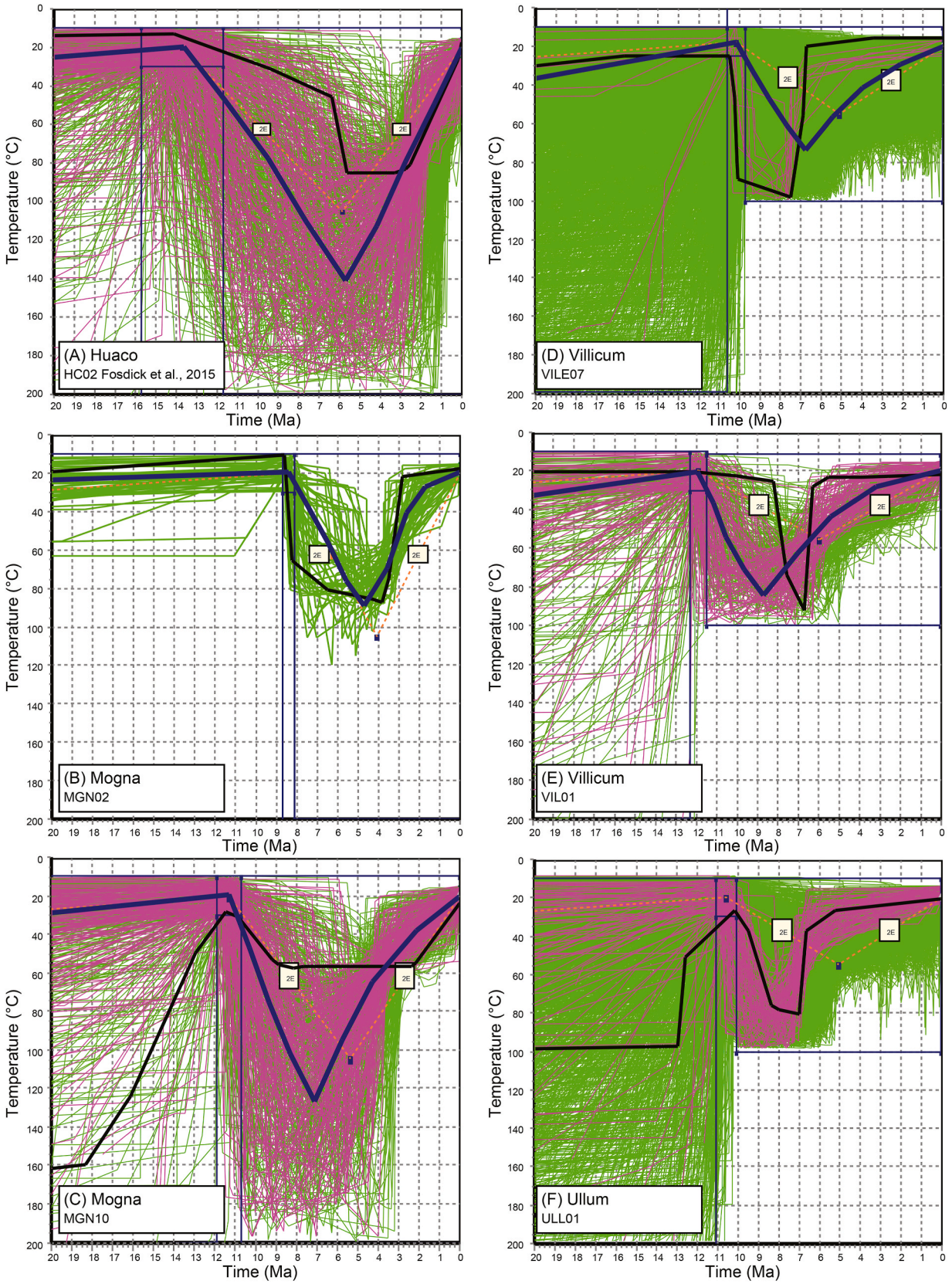

Fig. 8. Inverse thermal history modeling results for Miocene sandstone samples from the Bermejo basin using HeFTy software (Ketcham, 2005). (A) Huaco section. (B) Northern Mogna anticline. (C) Southern Mogna anticline. (D) Villicum section in central Sierra Villicum. (E) Southern Sierra Villicum. (D) Ullum section in northern Sierra Chica de Zonda. Time-temperature paths are colored as acceptable (green), good (purple), average (blue) and best fit (black).

2016), 240–285 Ma granitoids and silicic volcanics of the Choiyoi igneous province, and 225–240 post-Choiyoi igneous rocks (Mpodozis and Kay, 1992; Kleiman and Japas, 2009; Sato et al., 2015).

5. East-dipping subduction generated the Jurassic to Cenozoic Andean magmatic arc (0–200 Ma), which is defined by north-trending belts involving principally granite/granodiorite intrusions and andesite volcanics. These belts young systematically eastward from Jurassic (200–165 Ma) and Cretaceous (130–90 Ma) rocks along the Chilean coast, to Paleocene–Eocene (67–38 Ma) and Eocene–Oligocene (27–18 Ma) units along the western flank of the Principal Cordillera, and finally Miocene (17–4 Ma) volcanic rocks in the eastern Principal Cordillera, Frontal Cordillera, Precordillera and Sierras Pampeanas (Kay et al., 1991; Haschke et al., 2006; Jones et al., 2016; Capaldi et al., 2021).

4.4. Detrital Zircon U–Pb Age Results

Detrital zircon U–Pb age distributions from 14 sandstone samples from the Villicum and Ullum stratigraphic sections indicate ~7 million years of deposition in the Southern Bermejo basin and are plotted based on depositional age from oldest to youngest (bottom to top; Fig. 6). A summary of results is presented in the following paragraphs.

Samples from the Villicum stratigraphic section display an overall upsection increase in both Western and Eastern Sierras Pampeanas (early Paleozoic arcs) and Proterozoic basement age components during deposition from 13.3 to 5.7 Ma. All of the Villicum samples contain a significant amount of Andean Arc age grains ranging from 23 to 60%. Andean Arc age components show an initial decrease from 60% to 33% between 13.3 and 10 Ma. Andean Arc grains then increase and peak at 54% in the 7.6 Ma aged sample (VILE09), and then begin to decrease, reaching a minimum input of 23% at the top of the Villicum section (VILE11). Late Carboniferous to Triassic zircon age component is prevalent from 12.8 to 5.7 Ma, displaying two notable apparent maximums around 10 Ma (~40%) and 6.4 Ma (~20%). Western Sierras Pampeanas age components represent minor contributions throughout deposition of Villicum, showing an overall upward trend from <1% at the base of the section (VILE04) to ~9% at the end of deposition (VILE11). Eastern Sierras Pampeanas zircon inputs follow roughly the same trend as those of the Western Sierras Pampeanas, increasing from 0% at the start of deposition to a maximum of 18% at the top of the section. Proterozoic basement age components represent 28% of zircon composition at the base of the section in the 13.3 Ma aged sample, then show an initial decrease-reaching a minimum of 8% in the 8.7 Ma aged sample (VILE08). Proterozoic inputs then steadily increase and represent 24% of detrital zircon composition at the top of the section (VILE11).

Detrital zircon age distributions in the Ullum stratigraphic section reveal similar trends to those of Villicum. Contribution of Andean Arc age components are notable in every sample, ranging from 14% to 44%, with no observable pattern in terms of Andean Arc input throughout the duration of deposition. Late Carboniferous-Triassic grains represent a more consistent and dominant source of zircon grains for the Ullum section. There are two notable increases in Late Carboniferous-Triassic age components observed in the 10.1 Ma sample (ULL04) with 55% and at the top of the section (<6.5 Ma; ULL08) with 32%. These increases in Carboniferous-Triassic age components are also observed in coeval deposits in the Villicum section (Fig. 6). Western Sierras Pampeanas age components display an up-section decrease in relative contribution, from 29% in the 13.1 Ma aged sample (ULL02) to 7% in the two uppermost samples of the section (ULL07 & ULL08). Eastern Sierras Pampeanas aged zircon contributions are <10% in 4 lowest samples (ULL02-ULL05) and reach a maximum of 16% in the 6.8 Ma aged sample (ULL06), and then decrease to 10% at the top of the stratigraphic section.

5. Apatite (U–Th-Sm)/He Thermochronology

We conducted detrital apatite (U–Th-Sm)/He thermochronology analyses (AHe) to track the timing of tectonic and erosional exhumation in the Eastern Precordillera. We collected seven sandstone samples from the Mogna, Villicum, and Ullum stratigraphic sections (Fig. 2). Samples were targeted from basal deposits along each stratigraphic section, which are expected to record the highest degree of thermal resetting due to burial of overlying basin sediment. AHe thermochronometry relies on the temperature-dependent retention and diffusive loss of alpha particles (^{4}He) during the radioactive decay of U, Th, and Sm (Farley, 2002). The AHe system is characterized by its relatively low closure temperature, which ranges between ~30 and 90 °C depending on radiation damage accumulation, grain size, and composition of the crystal (Shuster et al., 2006; Flowers et al., 2009), corresponding to exhumation from ~1 to 4 km depth assuming a geothermal gradient of 20–26 °C/km in the Sierras Pampeanas continental crust (Sobel and Strecker, 2003; Löbens et al., 2013; Collo et al., 2017). Exhumational cooling is often delayed after tectonic activity, and thermochronometric data cannot directly quantify fault activity/uplift. However, if cooling is linked to fault-induced displacement and enhanced erosion, AHe ages may serve as a proxy for deformational timing (Ault et al., 2019; Mackaman-Lofland et al., 2020, 2022).

5.1. Methodology

Standard mineral separation was conducted on seven Miocene sandstone samples from foreland deposits exposed along the Eastern Precordillera, which included crushing, grinding, water table, heavy-liquid density, and magnetic susceptibility separations. Apatite grains were handpicked using an optical microscope, targeting non-broken, inclusion-free grains and were measured to calculate the grain mass and alpha ejection correction factor (Farley, 2000; Elhers and Farley, 2003). Single apatite grains were packed into platinum tubes, heated with a diode laser for 10 min at 1070 °C, and repeatedly reheated until the ^{4}He yield dropped to <1% to ensure complete degassing. Extracted gas was spiked with a ^{3}He tracer, cryogenically concentrated and purified, and measured with a noble gas quadrupole mass spectrometer at the University of Texas at Austin UTChron laboratory. Apatite aliquots were dissolved using HNO_3-based solution (diluted and purified MilliQ water to 5% HNO_3) spiked with ^{235}U, ^{230}Th, and ^{149}Sm tracers. Apatite U, Th, and Sm parent concentrations were measured by isotope dilution-inductively coupled plasma-mass spectrometry (ID-ICP-MS) analysis with a single-collector, magnetic sector Element2 ICP-MS. Durango apatite were analyzed as independent unknowns to ensure data quality and age accuracy (Boyce and Hodges, 2005). Based on replicate analysis of the Durango apatite standards, analytical uncertainties for uncorrected AHe ages are estimated at 6% (2σ). Reduced (U–Th-Sm)/He data for all samples analyzed are available in Supplemental File 6.

5.2. Detrital Apatite Results

New AHe analyses of eight sandstone samples from the Mogna, Villicum, and Ullum sections were compared against maximum depositional ages generated from detrital zircon U–Pb analysis (Capaldi et al., 2020) and magnetostratigraphic chronologies (Johnson et al., 1986; Milana et al., 2003) to evaluate which AHe dates are younger than the depositional age and therefore partially to fully reset. Aliquots with anonymously low He concentrations compared to the whole suite of data (i.e., [He] <0.049 nmol/g), despite having similar eU, were excluded from the results and calculations (Supplemental File 6).

Four samples were analyzed from the Mogna section with two samples collected from the eastern hanging wall (MGN01 and MGN02) and two from the western footwall (MGN08 and MGN10) across the west vergent thrust propagation fold (Fig. 2). All samples are discussed in

increasing stratigraphic order (bottom to top). Basal sample MGN08 from the Rio Salado Formation and yields dispersed dates with two aliquots younger than the magnetostratigraphic age (~19 Ma) of 16.4 ± 1.0 Ma and 2.7 ± 0.2 Ma and older dates of 46.9 ± 2.8 Ma and 61.3 ± 3.7 Ma. Sample MGN10 yields four AHe aliquots that are younger than zircon MDA (11.2 ± 1.1 Ma) with AHe grain dates between 3.5 ± 0.21 and 7.0 ± 0.42 Ma, and an older outlier of 133.2 ± 8.0 Ma. Sample MGN01 has dates 33.9 ± 2.0 Ma and 23.9 ± 1.4 Ma that are older than the 7.8 ± 0.4 Ma MDA and not considered further in our discussion. Uppermost sample MGN02 yields three reset aliquots which yield single-grain dates of 2.1 ± 0.12, 2.4 ± 0.14, and 5.0 ± 0.3 Ma and two older dates of 31.6 ± 1.9 Ma and 31.0 ± 1.9 Ma.

Two samples from the Villicum locality include VILE07 from the measured section and VIL01 sampled from the southern tip of Sierra Villicum (Fig. 1). Four aliquots from sample VIL01 are reset and yield grain ages that range from 6.2 ± 0.37 to 7.9 ± 0.47 Ma, younger than the MDA 11.9 ± 1.0 Ma. Sample VILE07 produced two out of five grain ages younger than the corresponding zircon MDA of 10.0 ± 0.6 Ma, yielding single age grain dates of 6.3 ± 0.4 and 9.2 ± 0.6.

Single-grain dates from the basal Ullum sample ULL01 range from 5.5 ± 0.33 to 10.1 ± 0.61 Ma. The disperse ages suggest partial resetting of the sample, which is from the thinnest stratigraphic section in the study.

5.3. Thermal History Modeling

Thermal history modeling provides a quantitative evaluation of a t-T history for a sample given input data of AHe single grain ages, grain size, and effective uranium (eU; eU=U+0.235 Th) concentrations. Samples from the Mogna, Villicum, and Ullum sections were modeled using the HeFTy program (version 1.9.1; Ketcham, 2005). We used radiation damage–diffusivity kinetics for apatite after Flowers et al. (2009) (RDAAM) and the alpha ejection correction from Ketcham (2005). Effective uranium concentration (eU) and grain size are accounted for in the thermal history modeling kinetics (Farley, 2002; Flowers et al., 2009; Flowers and Kelley, 2011). All models were run using grains that were younger than the sample depositional age to capture the post-deposition thermal history of basin accumulation and subsequent exhumation. HeFTy models were run until either 100 good fit paths were produced or 30,000 possible t-T paths were explored. Constraint boxes were used in each model based on geologic observations in order to obtain geologically reasonable thermal histories. Initial constraints include large constraint boxes ranging from 10° to 250 °C during 300 Ma to the samples maximum depositional age that enable, but do not require, the inverse model to explore non-monotonic time-temperature paths (e.g., paths that may reheat rocks) for the detrital apatite grains prior to deposition. This allows the model to explore variable pre-depositional time-temperature paths that could involve full resetting, partial resetting, or long durations for apatite grains to accumulate radiation damage. Following deposition at Earth surface the final constraint box that allows the model to simulate reheating during sediment burial and subsequent cooling during exhumation of the basin centers varies along strike. This temperature range is consistent with previous estimates of Mesozoic and Cenozoic maximum temperatures (Fosdick et al., 2015; Ortiz et al., 2015, 2021) in the Bermejo basin and purposely exceeds the closure temperature of the AHe systems allowing the model to explore all possible thermal scenarios, while also allowing grains to accumulate radiation damage.

Miocene sandstone samples are constrained by maximum deposition age at surface temperatures of 10° ± 10 °C, and modern surface temperatures. Modeled Huaco and Mogna samples from the northern Bermejo sections include a broad constraint box with temperatures between 10 °C and 200 °C enables the model to explore paths consistent with sediment burial and reheating at any time between depositional age and 0 Ma (Fig. 8A, B, and 8C). Samples from Villicum and Ullum sections have maximum reheating temperatures of 100 °C between their depositional age and 0 Ma to that is consistent with stratigraphic thicknesses of ~2 km given Miocene to modern surface temperatures of 10° ± 10 °C and the regional geothermal gradient of ~20–26 °C (Fig. 8D, E, 8F). Model parameters are provided in Supplemental File 7 following the reporting protocols of Flowers et al. (2015).

5.4. Thermal History Modeling Results

New thermal history modeling of Miocene basin deposits supports asynchronous basin cooling along-strike (Fig. 8). Miocene cooling initiates in the southern basin samples between 8 and 7 Ma, whereas the modeled northern samples display cooling broadly <6 Ma. The thermal history model of the Huaco sample incorporates existing AHe ages of 2.7 ± 0.2 Ma and 2.0 ± 0.6 Ma (Fosdick et al., 2015) with a broad depositional age estimate of 13.7 ± 2.0 Ma from magnetostratigraphy (Johnson et al., 1986). The HeFTy model results display sample reheating to 80–180 °C from deposition until ~6 to 3 Ma, when cooling commences at a steady rate of 20–40 °C/Myr (Fig. 8A).

Models for the Mogna samples broadly show cooling before 5 to 4 Ma. Sample MGN02 only produced "acceptable" paths in the HeFTy model with reheating to ~60–100 °C between 8 and 4 Ma followed by rapid cooling between 4 and 2 Ma that subsequently decreases in cooling rate until the surface. Most of the "good" fit paths from the HeFTy model for Mogna sample MGN10 indicate reheating during 11 to 7 Ma to temperatures of 80–160 °C. Modeled cooling paths for sample MGN10 begin around 7 to 4 Ma with initially rapid cooling followed by lower rates of cooling between 3 and 0 Ma (Fig. 8C).

Villicum sample VILE07 only produced 10 "good" paths from the HeFTy model that record reheating to 80–100 °C by 8 Ma followed by rapid cooling between 8 and 7 Ma that transitions to slower cooling rates until 0 Ma (Fig. 8D). The HeFTy model results for sample VIL01 yielded reheating to 60–100 °C between 11 and 7 Ma followed by progressive cooling since ~8-7 Ma (Fig. 8E).

The HeFTy model thermal history for sample ULL01 from the Ullum locality displays reheating to 70–100 °C by 8 Ma that transitions to rapid cooling below 50 °C by 6 Ma (Fig. 8F). Between 6 and 0 Ma cooling rate decreases as the modeled paths reach near surface temperatures.

6. Provenance Synthesis

Here we integrate the stratigraphic trends in paleocurrent variability and sediment provenance change using detrital zircon U–Pb age populations, and conglomerate clast counts to provide insight into erosional and related along-strike evolution of deformation and associated foreland basin development. Previously published detrital zircon age distributions from Huaco (Fosdick et al., 2015; Amidon et al., 2017) and Mogna (Capaldi et al., 2020) are plotted in Fig. 9.

Paleocurrent measurements from the Villicum and Ullum sections (Fig. 4) both records east-southeast directed sediment dispersal patterns, which suggest primarily western sediment source regions (i.e., Frontal Cordillera and Precordillera) during the Miocene and Pliocene. Paleocurrent measurements from the Huaco section also record southeast to east directed flow (Jordan et al., 2001). In the Mogna section, paleocurrent measurements from the basal deposits indicate an initial northwest directed flow that reversed up-section to an east directed flow throughout the Miocene and Pliocene (Capaldi et al., 2020).

The Ullum and Villicum stratigraphic sections incorporate a range of Andean arc zircons (0–200 Ma), comprising 24–60% at the Villicum section and 14–43% for the Ullum section. Notably, >90% of grains within the Andean arc age component are quite young, ranging between Oligocene-Pliocene (32-4 Ma) time period. Neither of the southern Bermejo sections display consistent or obvious up-section trends in terms of Andean arc derived zircons, however, consistent incorporation of these young (Oligocene-Pliocene) grains likely reflects continuous arc magmatism (Kay and Mpodozis, 2001; Capaldi et al., 2021). The Cenozoic zircon age distribution in the Mogna stratigraphic section

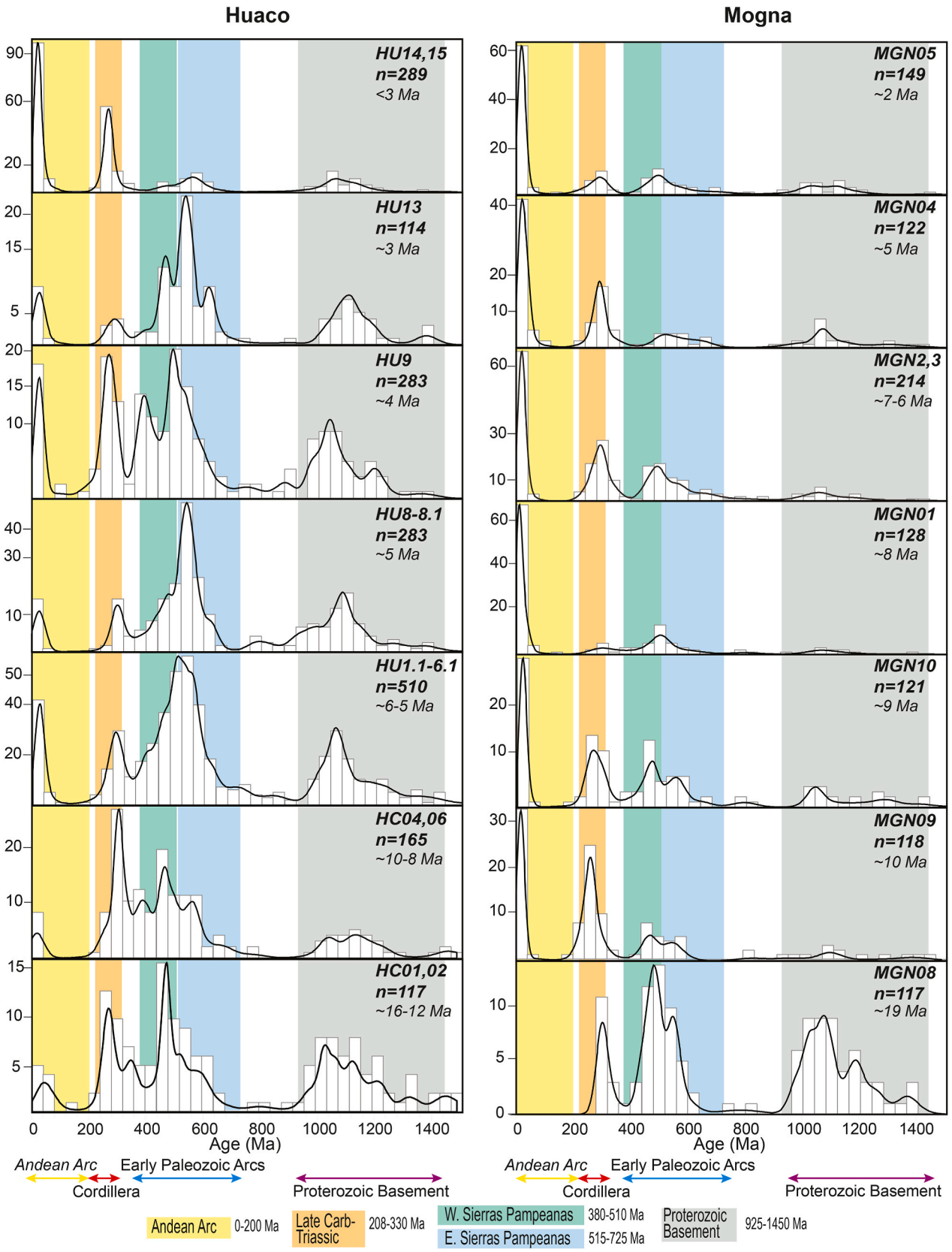

Fig. 9. Comparative plot of detrital zircon U–Pb age distributions for sandstone samples from the Huaco (Fosdick et al., 2015; Amidon et al., 2017) and Mogna (Capaldi et al., 2020) sections. Distributions depicted as kernel density estimates (20 Myr bandwidth) and age histograms with emphasis on key age components (color shading).

shows similar dominant contribution that is observed in the southern Bermejo sections, whereas the Huaco data displays the lowest proportion of Cenozoic ages (Fig. 9). In both northern and southern Bermejo basin localities there is an upsection shift from syn-deposition (<10 Ma) to older (10–45 Ma) Cenozoic age populations (Supplemental Fig. 1). The provenance trends likely represent shortening within the Precordillera thrust belt and associated erosional unroofing of recycled Cenozoic basin deposits (Capaldi et al., 2020).

Late Carboniferous to Triassic (225–330 Ma) aged zircon grains represent another steady contributor to Neogene basin fill of the Bermejo basin. Arc magmatism and crustal thickening (associated with input of the Andean arc zircons) was synchronous with deformation and erosion along the Frontal Cordillera (Fosdick et al., 2017; Buelow et al., 2018; Mackaman-Lofland et al., 2020). The deformation and associated erosion in the Frontal Cordillera likely exhumed Elqui-Limari and Choiyoi igneous rocks that acted as significant sediment sources to the Bermejo basin. There is a notable flux in late Carboniferous-Triassic zircons at 10 Ma (Figs. 6 and 9), potentially signaling a pulse of Frontal Cordillera deformation at this time. Another source of these grains could be from a recycled zircon input from the actively deforming Cenozoic basin deposits (e.g., Precordillera basins studied by Vergés et al., 2001; Levina et al., 2014; Suriano et al., 2017), which incorporated significant proportions of Choiyoi-aged zircon grains. Felsic and mafic volcanic clasts are also steady contributors to the conglomerate units in Bermejo basin, which are diagnostic of erosion of late-Paleozoic and Miocene volcanic rocks of the Frontal Cordillera (Jordan et al., 1993). Conglomerate facies are dominated by volcanic clast compositions that range from 66% to 44% of total clast distributions, reach maximum input at 10 Ma, and generally decrease up-section, likely reflecting erosion of Paleozoic sedimentary successions found within the more proximal Precordillera and lower structural levels of the Frontal Cordillera sediment sources through time.

Metasedimentary and sandstone clasts record Precordillera deformation and represent the Paleozoic strata being unroofed and subsequently eroded and transported to the Bermejo basin. Paleozoic conglomerate clast compositions increase from ~30% to ~50% in southern Bermejo. The pronounced east directed paleocurrent data along the foreland basin indicate that detrital zircon age distributions >300 Ma are recycled from Paleozoic and Mesozoic strata that were initially derived from eastern Sierras Pampeanas sediment sources. Sierras Pampeanas aged zircons (380–725 Ma) generally increase up-section in the southern Bermejo basin except for the basal sample at Ullum (ULL02), which records an anomalously high percentage of Western Sierras Pampeanas grains at ~40% (Fig. 6). This anomaly likely reflects erosion of locally derived Paleozoic strata in the earliest stage of basin deposition at the Ullum locality. The up-section increase in Eastern and Western Sierras Pampeanas aged zircon populations is particularly evident in the Villicum section and is most likely a result of increased sediment contribution from the Precordillera associated with unroofing of Paleozoic strata (Jordan et al., 1993; Fosdick et al., 2015). Proterozoic basement zircons (925–1450 Ma) follow a similar trend to Pampean zircons in that they increase up-section. It is likely that Precordillera deformation also contributed Proterozoic aged zircons into the basin fill in southern Bermejo basin. Metasedimentary and red-brown-gray sandstone conglomerate clasts follow similar up-section trends to Paleo-Proterozoic detrital zircon provenance, generally increasing up-section (with a few internal cycles). Deposition of southern Bermejo basin sections is coeval with the initiation of deformation across the Precordillera and into the western-most foreland. The Precordilleran provenance signature is pervasive in the Huaco and Mogna detrital zircon age spectrum (Fig. 9), with strong contribution of early Paleozoic arc and Proterozoic basement age components.

6.1. Multidimensional Scaling Plot

We generated a MDS plot to examine the similarity among zircon provenance for each basin location (Fig. 10). New data from Villicum and Ullum are integrated with published detrital zircon U–Pb age datasets from the Mogna and Huaco sections (Figs. 6 and 9; Fosdick et al., 2015; Amidon et al., 2017; Capaldi et al., 2020). The DZ samples plotted in the MDS exhibit trends that indicate the positive y-space represents greater abundance of Paleozoic arc and Proterozoic basement aged zircons; positive x-space represents greater influence of Choiyoi and Elqui-Limari arc diagnostic ages; and negative x-space represents greater incorporation of Andean Arc-aged zircon grains. Each U–Pb age distribution is also annotated with the approximate depositional age of the given sample, adding a time component to the plot (Fig. 10).

The MDS plot reveals several distinct spatial and temporal trends among the four stratigraphic sections indicating drainage connectivity or isolation during the foreland basin development. The samples from the Huaco section (Fig. 10; blue) plot further away from the other three sections, dictated by the strong older Paleozoic arcs and Proterozoic basement source age component observed in these samples. The cluster of Huaco samples in MDS space suggests that the Huaco deposits recorded a unique sediment source that is fluvially disconnected from southern Bermejo basin. This sediment source was likely being fed by catchment areas predominately comprised of Ordovician and Carboniferous-Permian siliciclastic strata that recycled Pampean-Proterozoic zircons during northern Precordillera deformation, signaling a greater contribution of these grains in the north (Fig. 1). The basal Mogna (Fig. 10; red) and Ullum (Fig. 8; yellow) samples also plot in the Pampean-Proterozoic basement MDS space, suggesting that local Paleozoic and basement sources that underlie the deposits were contributing sediment in the initial basin formation phase. Both the Mogna and Villicum (Fig. 10; red and green) samples overlap predominantly in the negative-x MDS space, indicating a shared sediment source dominated by Andean arc derived grains. The amount of overlap observed between the zircon U–Pb age distributions of Mogna and Villicum after 10 Ma implies that these sections were fluvially connected and tapping into an eroding Andean arc source. The dominant young (Oligocene-Pliocene) aged zircon being sourced to this Neogene basin fill suggest that the fluvial system feeding Mogna and Villicum was

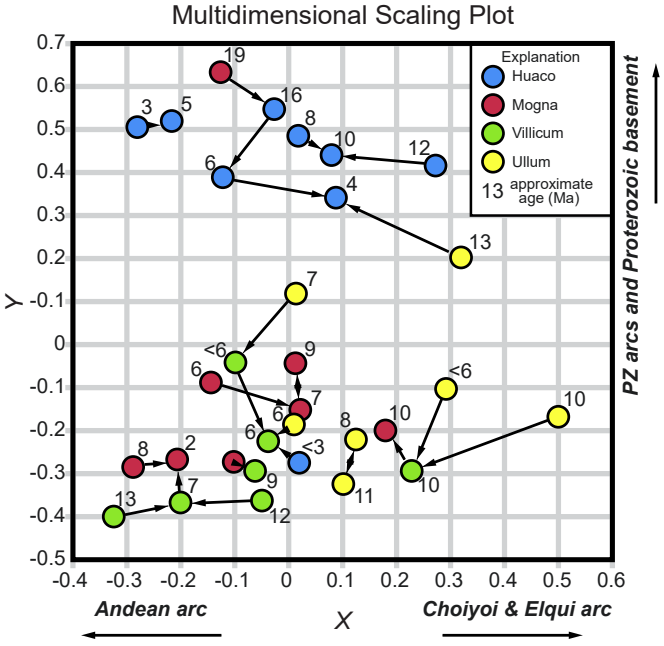

Fig. 10. Three-dimensional multidimensional scaling (MDS) plot of DZ U–Pb age distributions generated for sandstone samples using KDE (20 Myr bandwidth) and R^2 cross-correlation coefficient test. Lines represent nearest neighbor (black arrows). Axes are unitless with age distribution data trends on X and Y axis inferred (black arrows).

tapping into Cenozoic basins of the Precordillera which began deforming between 12 and 9 Ma (Jordan et al., 1993; Levina et al., 2014). The Ullum samples plot towards the positive x-space, suggesting a system that is more dominated by Carboniferous-Triassic (Choiyoi & Elqui-Limari arc) sources. There is a fair amount of overlap between the Mogna and Villicum system with Ullum, indicating that these sections experienced similar sediment provenance histories. However, Ullum experiences a greater influence of sediment input from the Choiyoi and Elqui arcs suggesting that the system feeding into Ullum was fluvially disconnected from the source feeding Mogna and Villicum. Since sediment was depositing in the Ullum locality at roughly the same time as Villicum (13-6 Ma), this may suggest that the source for Ullum was a southern Cenozoic basin with a unique depositional history (e.g., Albarracín studied by Vergés et al., 2001; Levina et al., 2014) which incorporated significant proportions of Choiyoi-Elqui igneous rocks. The observed along-strike differences in sediment provenance during Bermejo basin deposition is a direct result of the along-strike complexities seen within the deforming Precordillera coeval with deposition in the foreland.

7. Basin Subsidence and Thermal History

Integration of new detrital zircon U–Pb geochronologic time constraints (MDAs) from the Villicum and Ullum sections paired with published magnetostratigraphic data for the Huaco (Johnson et al., 1986) and Mogna (Milana et al., 2003) sections allows for a reconstruction of along-strike sediment accumulation histories of the Bermejo basin (Fig. 9). The stratigraphic age and thickness data reveal a distinct

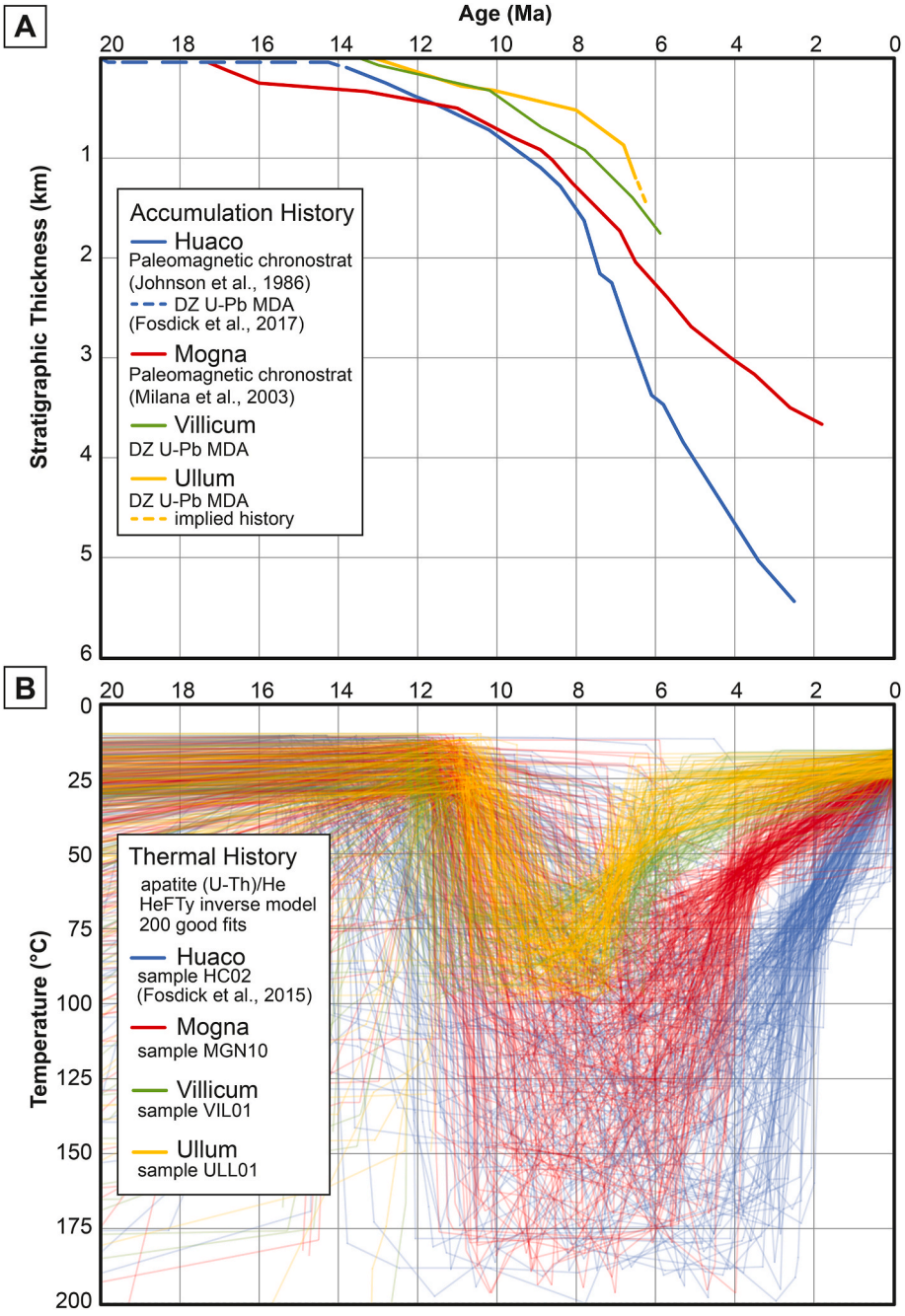

Fig. 11. Along-strike Bermejo basin accumulation and thermal history. (A) Sediment accumulation plots recording time-transgressive basin initiation from north to south. (B) Time-temperature plots of Miocene basin deposits recording time-transgressive basin exhumation from south to north.

along-strike difference in sediment accumulation histories in the northern (Huaco, Mogna) versus southern Bermejo basin (Villicum, Ullum). First order observations show a decrease in stratigraphic thicknesses from north to south. Huaco, at the northern extent of our study, has a thickness greater than 5 km, while Ullum, at the southern extent, is less than 2 km thick (Fig. 11).

Sediment accumulation rates can be a useful tool for informing depositional environments, especially in a foreland basin system with well-defined depositional zones. In the early stages of deposition in the northern Bermejo basin (18-13 Ma), the Huaco and Mogna sections record low rates of sediment accumulation of 38 m/Myr (Huaco) and 75 m/Myr (Mogna). Low sediment accumulation rates at this time likely signify deposition in the distal foreland basin depositional zone (Flemings and Jordan, 1989; DeCelles and Burden, 1992). Between 13 and 9 Ma, the accumulation rate in northern Bermejo increases to 234 m/Myr (Huaco) and 143 m/Myr (Mogna). Sediment begins to accumulate in the southern Bermejo basin at this time with rates of 190 m/Myr in Villicum and 112 m/Myr in Ullum. Maximum sediment accumulation rates occur between 9 and 5 Ma across the entire Bermejo foreland basin with observed rates of: 768 m/Myr in Huaco, 463 m/Myr in Mogna, 338 m/Myr in Villicum, and 263 m/Myr in Ullum. The increase in sediment accumulation rate through time signals a transition into a foredeep depositional zone of the evolving foreland basin system (DeCelles and Giles, 1996). In the final stage of basin development (5-0 Ma), sediment continues to accumulate in Huaco and Mogna until 2 Ma with decreased rates of 400 m/Myr at Huaco and 281 m/Myr at Mogna. Deposition in the southern Bermejo basin ceased during this stage. These decreased rates of sediment accumulation indicate a more proximal orogenic wedge and a switch to wedge-top deposition as the topographic front and associated foreland basin system continued to migrate eastward

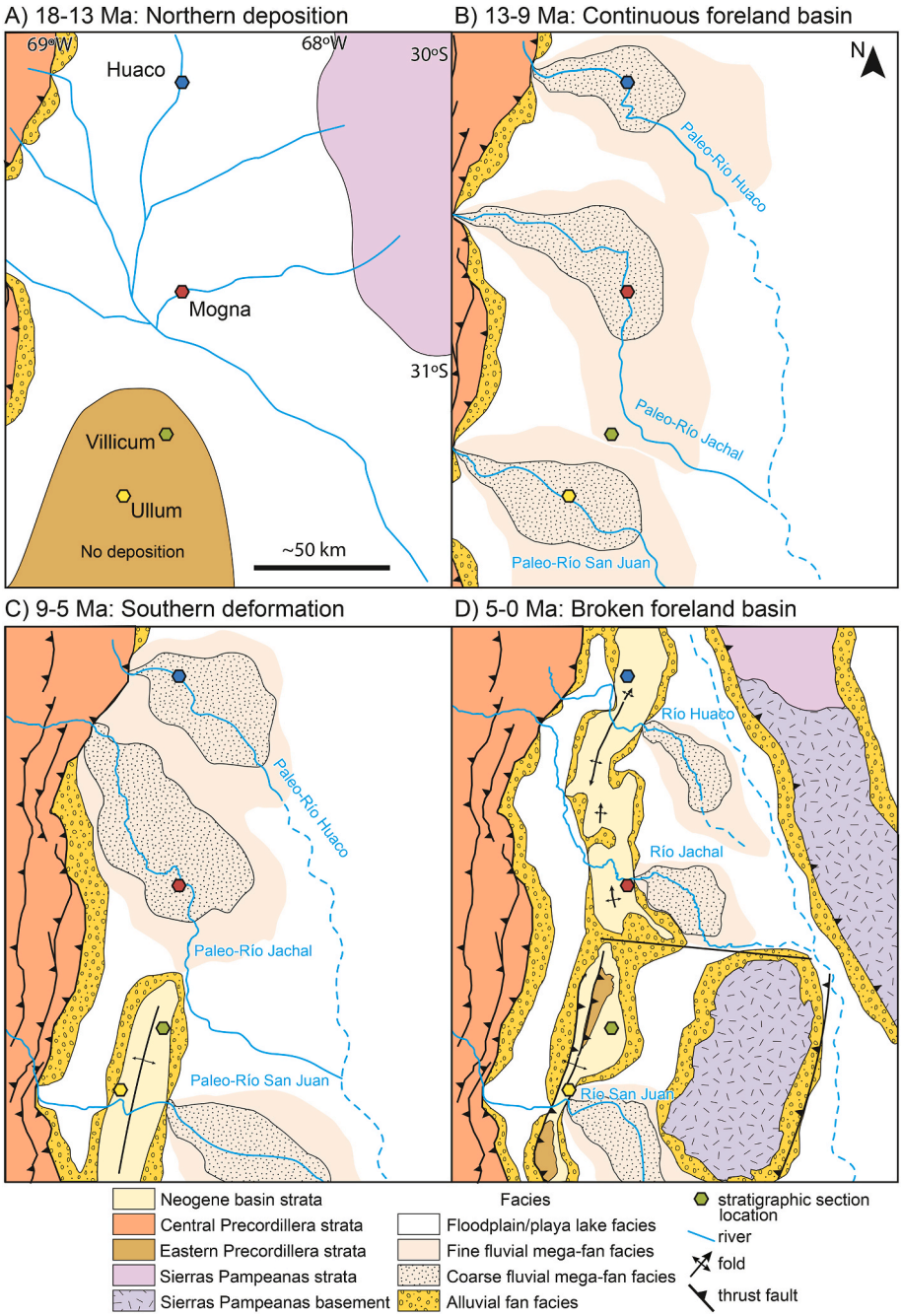

Fig. 12. Paleogeographic reconstructions of Bermejo basin between 18 and 0 Ma.

(Allmendinger and Judge, 2014; Fosdick et al., 2015; Mardonez et al., 2020; Mackaman-Lofland et al., 2022).

New AHe data and inverse thermal history models from Mogna, Villicum, and Ullum localities along with published ages from Huaco (Fosdick et al., 2015), reveal two distinct phases of exhumation along the Eastern Precordillera (Fig. 11B). Collectively, the good fit t-T paths show a northward migration in basin cooling that initiates in southern Bermejo between 8 and 6 Ma followed by a second phase during 5–2 Ma in northern Bermejo. Basin reheating for each locality is coeval with sediment accumulation with greater reheating modeled for the northern basin sections owing to the fact these localities preserve thicker Miocene deposits. When stratigraphic age, thickness, and exhumation data are plotted together (Fig. 11), it becomes evident that the termination of deposition in the northern and southern stratigraphic sections aligns well with initiation of exhumation in the Eastern Precordillera. In the southern Bermejo basin sediment accumulation ends around 6 Ma, coeval with basin cooling that is interpreted to be driven by shortening along the Eastern Precordillera. In contrast, in the northern Bermejo basin sediment accumulation continued until ~2 Ma. The t-T histories for the Mogna and Huaco localities reveal exhumation-related cooling to converge at 4 Ma until present day for Mogna and 3 Ma to present day for Huaco. Collectively, basin initiation occurs first in the north in the early Miocene and the south in the middle Miocene, and subsequent basin exhumation occurs first in the south by the late Miocene and then the north by the Pliocene.

8. Discussion

The combination of stratigraphic (Fig. 4), lithofacies (Table 1), provenance (Figs. 6, 9 and 10), sediment accumulation, and basin thermal histories (Fig. 9) provide insights into Andean unroofing patterns and the related depositional and deformational variations along strike within the Bermejo basin. We identify four key timesteps in the evolution of the Bermejo foreland basin: (1) Early to middle Miocene, 18-13 Ma; (2) Middle to Late Miocene, 13-9 Ma; (3) Late Miocene to early Pliocene, 9-5 Ma; and (4) Pliocene to present, 5-0 Ma (Fig. 12).

8.1. Early-Middle Miocene Northern Deposition

The early-middle Miocene stage of foreland basin development (18-13 Ma) is concentrated in northern Bermejo basin with basal depositional ages of 16 Ma and 17 Ma for Huaco and Mogna, respectively (Fosdick et al., 2015; Milana et al., 2003; Mackaman-Lofland et al., 2022). Early sediment accumulation occurred at very low rates (<80 m/Myr) in the northern Bermejo basin, which recorded the initial development of the flexural foreland basin initiated by uplift of the Frontal Cordillera and the eastward advance of the Precordillera thrust front (Fernandez and Jordan, 1996; Jordan et al., 1993; Milana et al., 2003). Sedimentological analyses of early-middle Miocene strata suggest earlier eolian depositional environments with a switch to more fluvially dominated systems by 13 Ma, as preserved in the Rio Salado and Quebrada del Jarillal Formations (Fig. 3; Fernandez and Jordan, 1996; Jordan et al., 2001). The southern Bermejo basin recorded no sediment accumulation at this time, defining a non-depositional zone south of 31°S in the Bermejo basin (Fig. 12A). Southwest of the inactive southern Bermejo basin (Ullum and Villicum), the Miocene Albarracin basin began accumulating sediment at 18-16 Ma (Levina et al., 2014; Vergés et al., 2001). This indicates that deposition was occurring south of 31°S, but not in the easternmost reaches of the Eastern Precordillera in the southern Bermejo basin at Ullum and Villicum. Early to mid-Miocene paleocurrent data indicate northwest directed flow for the Mogna section (Capaldi et al., 2020) and southwest directed flow for the Huaco section (Fosdick et al., 2017), suggesting initial sediment sources from the eastern cratonic margin and overlying Carboniferous to Triassic strata. Evidence of very low sediment accumulation rates for sediments derived from eastern cratonic sources suggests deposition in the distal foreland depositional zone of a foreland basin system (DeCelles and Giles, 1996). The lack of sediment accumulation in the southern Bermejo basin between 18 and 13 Ma suggests that either: (1) early exhumation in the Western-Central Precordillera and associated flexural subsidence was concentrated north of 31°S, and/or (2) the southern Eastern Precordillera remained a paleo-topographic high at this time. The lack of deposition south of 31°S coincides with the North Pie de Palo fault, which may be an inherited structural feature of the Protoprecordillera that remained a structural high due to Ancestral Andean Mountain building throughout the Paleozoic (Limarino et al., 2001). The lack of Carboniferous to Paleogene deposits in the southern Eastern Precordillera beneath the southern Bermejo basin, in contrast to the presence of deposits of these ages beneath strata of the northern Bermejo basin, supports the interpretation that the pre-Andean foreland configuration was spatially variable and imparts a structural control on initial basin formation.

8.2. Mid-Late Miocene Continuous Foreland Basin

The mid-late Miocene (13-9 Ma) phase in Bermejo basin development is marked by an increase in fluvial activity across the region and a notable reversal in paleocurrents from northwest-southwest to south-southeast directed flow at Mogna and Huaco (Capaldi et al., 2020; Fosdick et al., 2017) and the beginning of south-southeast directed flow at Villicum and Ullum. The Villicum and Ullum sections of southern Bermejo begin accumulating sediment at 13 Ma, coinciding with the advance of the fold-thrust belt from the Western Precordillera into the Central Precordillera between 14 and 9 Ma (Fernandez and Jordan, 1996; Jordan et al., 1993; Milana et al., 2003; Levina et al., 2014). Depositional environments reflect ephemeral lake systems and distal floodplains that progressively grade into thicker and sandier fluvial facies recorded in the Lomas de las Tapias, Quebrada del Jarillal, Huachipampa, and Quebrada del Cura Formations. All four along-strike sections within the Bermejo basin experience relatively moderate sediment accumulation rates (~100–200 m/Myr) during the mid-late Miocene (Fig. 9). Both Huaco and Mogna stratigraphic sections record an increase in sediment accumulation rates relative to pre-13 Ma rates, reflecting increased shortening in the Precordillera and associated flexural subsidence (Allmendinger and Judge, 2014; Mardonez et al., 2020; Mackaman-Lofland et al., 2022). Moderate sediment accumulation rates and the occurrence of regional fluvial activity sourced from western Andean regions indicates persistent accumulation in the distal foredeep depozone of the evolving foreland basin system (Fernandez and Jordan, 1996; DeCelles and Giles, 1996). The middle to late Miocene Bermejo basin experienced a notable increase in late Carboniferous-Triassic aged zircon input and high contribution of felsic-mafic volcanic clasts, likely reflecting erosion of Frontal Cordillera sources and unroofing of foreland basin deposits across the Precordillera, resulting in the recycling of Andean arc and hinterland sediment signatures. Structural and thermochronological constraints from the hinterland indicate that accumulating sediment in the Bermejo basin is being sourced from both the Frontal Cordillera and Precordillera ((Allmendinger and Judge, 2014); Fosdick et al., 2015; Mardonez et al., 2020; Mackaman-Lofland et al., 2020, 2022).

8.3. Late-Miocene to Early-Pliocene Southern Deformation

The end Miocene-early Pliocene time (9-5 Ma) in the Bermejo basin is distinguished by increased sediment accumulation rates across the entirety of the foreland basin (~300 m/Myr in southern Bermejo to ~800 m/Myr in northern Bermejo). The observed contemporaneous increase in sedimentation rates at Huaco and Mogna (Fernandez and Jordan, 1996), and Villicum and Ullum indicates regionally synchronous shortening and thrust loading over 100 km along-strike in the Central Precordillera (Jordan et al., 2001). Changes in lithofacies at Villicum and Ullum during this phase of basin development reflects the

eastward advance of the Precordillera fold-thrust belt via increasingly coarser-grained sediments which is interpreted as a transition from avulsing sandy channels on a distal flood-plain to a higher-energy braided system and eventual incorporation of debris flow deposits (Upper Lomas de las Tapias, Mogna and El Corral Formations). Facies analyses of the Villicum and Ullum sections lead us to interpret the up-section trends as deposition and migration of a fluvial megafan that is being sourced from the actively deforming Precordillera thrust belt. Analysis of correlative formations in the northern Bermejo basin have been interpreted as proximal alluvial fan and bajada depositional environments (Fernandez and Jordan, 1996; Johnson et al., 1986; Jordan et al., 1993), however we suggest that they may be a part of the separate fluvial megafan system. High sediment accumulation rates, paired with sediment sourced directly from the approaching fold-thrust belt and dominant fluvial megafan facies, implies that deposition occurred in the foredeep depozone of the foreland basin system at this time (DeCelles and Giles, 1996; Flemings and Jordan, 1989). By 6.5 Ma, southern Bermejo basin (Villicum and Ullum) transitioned to wedge-top environments, as supported by the predominantly coarse-grained conglomerate facies (Mogna and El Corral Formations; DeCelles and Giles, 1996), before being exhumed by thrust belt shortening by 5 Ma. Detrital zircon U–Pb age distributions reflect an increase in Paleozoic-Proterozoic age components indicative of unroofing and sediment derivation from recycled Paleozoic sources in the Precordillera. Our new AHe data from the southern Bermejo sections reflect exhumation between 7 and 5 Ma, while at this time the northern Bermejo basin continued to accumulate sediment in broad fluvial megafan depositional environments. The 3–5 Myr difference in the time of exhumation between the southern and northern Bermejo basin implies asynchronous evolution of the retroarc basin system, where deformation initiates in the Eastern Precordillera around 6 Ma in Ullum and Villicum. As a result of the evolving Eastern Precordillera thrust front, broad synclinal structures perturbed the Ullum and Villicum localities leading to the exhumation of the southern Bermejo basin strata.

8.4. Pliocene to Present Broken Foreland Basin

The final phase of Bermejo basin development (5-0 Ma) is distinguished by basement-involved shortening in the foreland and consequent uplift of the Sierras Pampeanas, resulting in the present day broken-foreland basin system (Jordan and Allmendinger, 1986; Jordan et al., 2001; Horton et al., 2022a). Sediment accumulation continued at Huaco and Mogna until 4-2 Ma, with rates decreasing from the main phase of accumulation (9-5 Ma) to ~400 and ~300 m/Myr for Huaco and Mogna, respectively. Relatively high accumulation rates suggest continued deformation in the Precordillera, however the decrease in rates from the previous phase likely tracks the encroachment of the thrust front and deposition in the wedge-top foreland basin depozone (DeCelles and Giles, 1996). Deposition in the northern Bermejo basin is dominated by thick conglomeratic facies (Mogna and El Corral Formations) corresponding to proximal river dominated fans (Fernandez and Jordan, 1996; Jordan et al., 1993; Milana et al., 2003), which we interpret as likely fluvial megafan systems. Northern Bermejo exhumation was coeval with uplift of the Sierras Pampeanas (Ortiz et al., 2015, 2022; Mackaman-Lofland et al., 2022). Published AHe ages for the Huaco section suggest uplift at 2 Ma (Fosdick et al., 2015) and new data from the Mogna section shows exhumation initiating by 3.5 Ma, at which point the northern Bermejo basin was incorporated into the Eastern Precordillera fold-thrust belt, forming the broad anticlinal structures observed today at Mogna and Huaco (Fig. 11). The contemporaneous deformation of the northern Bermejo basin and thick-skinned Sierras Pampeanas supports the interpretation that the northern Eastern Precordillera may be kinematically linked to the deep-rooted thrust structures of the Sierras Pampeanas, as previously suggested (e.g., Zapata and Allmendinger, 1996; Zapata, 1998; Mardonez et al., 2020). The earlier uplift of the southern Bermejo (>5 Ma) leads us to conclude that there are complex along-strike variations in the Eastern Precordillera thrust-front evolution, and that the southern Bermejo basin may not be structurally linked to the deep-rooted Sierras Pampeanas, as previously suggested (Ramos et al., 2002, 2009; Siame et al., 2002, 2005; Vergés et al., 2007).

8.5. Along-strike Variations in Bermejo Basin Evolution

New sedimentological, geochronologic, and thermochronologic datasets provide quantitative evidence of the variability that exists in retroarc foreland basin development and thrust-front evolution in the south-central Andes between 30 and 32°S. The Bermejo basin developed discontinuously along strike, with deposition initiating around 24-18 Ma (Johnson et al., 1986; Milana et al., 2003) in the north and by 13 Ma in the south. This asynchronous north to south foreland basin initiation has been proposed to track spatially and temporally with the subduction of the Juan Fernandez ridge and associated flat slab geometry driving upper plate deformation above the flat slab (Beer and Jordan, 1989; Jordan et al., 1993, 2001; Ramos and Folguera, 2009; Vergés et al., 2001). Comparing distal stratigraphic records along-strike rather than across-strike proximal to distal comparisons (i.e., Capaldi et al., 2020; Mackaman-Lofland et al., 2020) provides better spatial constraints to track north-south time-transgressive changes in the foreland basin development. Our results show that the inherited pre-Andean paleo--topography and crustal structures may have inhibited southern Bermejo basin development. Neogene basin deposits west of the Villicum and Ullum localities are preserved in the Frontal Cordillera and Precordillera, and record basin initiation around 24-18 Ma (Vergés et al., 2001; Levina et al., 2014; Pinto et al., 2018; Mackaman-Lofland et al., 2020; Capaldi et al., 2020). This suggest that retro-arc deformation and associated flexural basin formation occurred over 350 km along-strike. Between 24 and 13 Ma the Huaco and Mogna localities reflect back bulge to distal foredeep basin depositional environments, whereas the southern Villicum and Ullum remained an erosional surface. This heterogeneity suggests the southern Bermejo region is either a remnant topographic high during initial phase of foreland basin development or records underfilled forebulge development that potentially removed older basin deposits until 13 Ma when Precordilleran deformation propagated eastward inducing sufficient flexural subsidence in the southern region to initiate basin development. Following a phase of integrated foreland basin development, the along-strike shortening-induced exhumation of basin deposits was diachronous above the Eastern Precordillera. Southern Bermejo basin deposits experienced exhumation driven cooling between 8 and 6 Ma that propagated northward along the Eastern Precordillera by 5 to 2 Ma as the proximal Bermejo basin was incorporated into the orogenic wedge. The contrasting timing of both basin initiation and exhumation occurs across the North Pie de Palo fault, suggesting that inherited structures associated with Ancestral Andean deformation imparts a direct control on retro-arc basin evolution.

9. Conclusions

The Bermejo retroarc foreland basin formed as a flexural response to Miocene crustal thickening in the Andean orogenic system. The well-preserved stratigraphy of Neogene basin deposits in the Bermejo basin provides an opportunity for an along-strike analysis of the evolution of the adjacent Eastern Precordillera and overall foreland basin-broken basin development in a modern flat-slab subduction region. Integration of new and published datasets allows for a temporal and spatial analysis of basin development and deformation to understand the variability in an evolving thrust front.

1. Published data from northern Bermejo basin deposits places temporal constraints on deposition between 20 and 2 Ma, while new data from southern Bermejo basin deposits indicate deposition from 13 to

6 Ma. The northern Bermejo basin experienced a longer-duration depositional history, accumulating thicker stratigraphic sections (>4 km) than in the south (<2 km).

2. Facies analyses of southern Bermejo stratigraphy identify upward coarsening sequences dominated by thick, multistoried, laterally continuous sand channels with flat bottoms, interbedded with mud-siltstone floodplain and overbank facies that are capped by thick conglomerate braided river channels. This stratigraphic succession is interpreted to represent a fluvial megafan sequence being sourced by the Precordillera and Andean hinterland. The upward coarsening and thickening trend of stratigraphic sections tracks the migration of the fluvial megafan system as the Precordillera thrust-front propagates into the foreland.
3. Detrital zircon U–Pb geochronologic analyses paired with conglomerate clast composition datasets provide insight into sediment provenance through time, which can detect deformation and erosion of distinct source areas. Up-section trends of significant pulses of certain age components and clast lithologies inform on regional deformation. In the southern Bermejo basin, provenance synthesis shows up-section increases in both Paleoproterozoic zircon age components, and Paleozoic metasedimentary and sedimentary conglomerate clasts, indicating a pulse of Precordillera deformation between 13 and 6 Ma. There is also a notable increase in late Carboniferous-Triassic aged zircons and a high percentage of volcanic conglomerate clasts by 10 Ma, which signals a pulse of exhumation in the Frontal Cordillera, and erosion of Cenozoic basin deposits within the Precordillera.
4. New AHe data for northern (Mogna) and southern (Villicum and Ullum) Bermejo basin localities, along with published AHe ages for Huaco show two distinct pulses of exhumation related cooling in the Bermejo basin. The Eastern Precordillera fold-thrust belt deformation incorporated the southern Bermejo basin strata at 6 Ma. Eastern Precordillera exhumation migrated northward to the Mogna locality at 3.5 Ma and to the Huaco section by 2 Ma. The time-transgressive trend in exhumation along strike of the Bermejo basin implies diachronous deformation of basin deposits.
5. Combined analysis of sedimentologic, geo-/thermochronologic, and basin history data suggest that the along-strike evolution of the Bermejo foreland basin system has been asynchronous through time. The diachronous basin history is not a direct response to external drivers such as southward migration of flat slab subduction, but rather reflects the importance of preexisting structural fabrics that underly the retro-arc foreland basin system during Andean orogenesis.

CRediT authorship contribution statement

Zoey C. Plonka: Conceptualization, Investigation, Writing, Visualization. **Tomas N. Capaldi:** Conceptualization, Investigation, Writing, Visualization. **Margaret L. Odlum:** Conceptualization, Investigation, Writing. **Chelsea Mackaman-Lofland:** Conceptualization, Investigation, Writing. **Gustavo Ortiz:** Conceptualization, Investigation, Writing. **Patricia Alvarado:** Conceptualization, Investigation, Writing

Declaration of competing interest

The authors declare that they have no known competing financial interests or personal relationships that could have appeared to influence the work reported in this paper.

Data availability

Data will be provided in supplemental files.

Acknowledgments

We are grateful for the essential role Patricia Alvarado played in all of our studies in Argentina, and as a friend and mentor. She dedicated her career to unraveling the structural complexities of the Andes to better scientific knowledge, but most importantly to better her community. This research was supported by U.S. National Science Foundation grant (EAR-2242878) awarded to T.N. Capaldi, M.L. Odlum, and C. Mackaman-Lofland, and student research support from the Geological Society of America awarded to Z.C. Plonka. We thank Brian Horton, Facundo Fuentes, Ryan McKenzie, Daniel Starck, Daniel Stockli, Lisa Stockli, Michael Wells, Kevin Konrad, and Rudra Chatterjee for helpful discussions and analytical assistance. We appreciate the constructive reviews from Julieta Suriano and an anonymous reviewer that significantly improved the manuscript.

Appendix A. Supplementary data

Supplementary data to this article at geochron.org (http://www.geochron.org/results.php?pkey=41032) and can be found online at https://doi.org/10.1016/j.jsames.2023.104521.

References

Allmendinger, R.W., Judge, P.A., 2014. The Argentine Precordillera: a foreland thrust belt proximal to the subducted plate. Geosphere 10, 1203–1218. https://doi.org/10.1130/GES01062.1.

Allmendinger, R.W., Figueroa, D., Snyder, D., Beer, J., Mpodozis, C., Isacks, B.L., 1990. Foreland shortening and crustal balancing in the Andes at 30S Latitude. Tectonics 9, 789–809.

Allmendinger, R.W., Cardozo, N., Fisher, D., 2012. Structural Geology Algorithms: Vectors and Tensors in Structural Geology. Cambridge University Press (book to be published in early 2012).

Alvarado, P., Beck, S., 2006. Source characterization of the san juan (Argentina) crustal earthquakes of 15 january 1944 (MW 7.0) and 11 june 1952 (MW 6.8). Earth Planet Sci. Lett. 243 (3–4), 615–631.

Alvarado, P., Pardo, M., Gilbert, H., Miranda, S., Anderson, M., Saez, M., Beck, S., 2009. Flat-slab subduction and crustal models for the seismically active Sierras Pampeanas region of Argentina. CO. In: Kay, S.M., Ramos, V.A., Dickinson, W.R. (Eds.), Backbone of the Americas: Shallow Subduction, Plateau Uplift, and Ridge and Terrane Collision, vol. 204. Geological Society of America Memoir, USA, pp. 261–278. https://doi.org/10.1130/2009.1204(12.

Amidon, W.H., Fisher, G.B., Burbank, D.W., Ciccioli, P.L., Alonso, R.N., Gorin, A.L., et al., 2017. Mio-Pliocene aridity in the south-central Andes associated with Southern Hemisphere cold periods. Proc. Natl. Acad. Sci. U. S. A. 114, 6474–6479. https://doi.org/10.1073/pnas.1700327114.

Ault, A., Gautheron, C., King, G., 2019. Innovations in (U-Th)/He, fission-track, and trapped-charge thermochronometry with applications to earthquakes, weathering, surface-mantle connections, and growth and decay of mountains. Tectonics 38 (11), 3705–3739. https://doi.org/10.1029/2018TC005312.

Bahlburg, H., Vervoort, J.D., Du Frane, S.A., Bock, B., Augustsson, C., Reimann, C., 2009. Timing of crust formation and recycling in accretionary orogens: insights learned from the western margin of South America. Earth Sci. Rev. 97, 215–241. https://doi.org/10.1016/j.earscirev.2009.10.006.

Barazangi, M., Isacks, B.L., 1976. Spatial distribution of earthquakes and subduction of the Nazca plate beneath South America. Geology 4 (11), 686–692. https://doi.org/10.1130/0091-7613(1976)4<686:SDOEAS>2.0.CO, 2.

Beer, J.A., Allmendinger, R.W., Figueroa, D.E., Jordan, T.E., 1990. Seismic stratigraphy of a Neogene piggyback basin, Argentina. AAPG bulletin 74 (8), 1183–1202.

Beer, J.A., Jordan, T.E., 1989. The effects of Neogene thrusting on deposition in the Bermejo Basin, Argentina. J. Sediment. Res. 59 (2), 330–345. https://doi.org/10.1306/212F8F8A-2B24-11D7-8648000102C1865D.

Bellahsen, N., Sebrier, M., Siame, L., 2016. Crustal shortening at the Sierra Pie de Palo (sierras Pampeanas, Argentina): near-surface basement folding and thrusting. Geol. Mag. 153, 992–1012. https://doi.org/10.1017/S0016756816000467.

Bercowski, F., Berenstein, L.R., Johnson, N.M., 1987. Litofacies y Paleoambiente del Terciario en Lomas de las Tapias, Ullum, Prov. de San Juan, Argentina. Decimo congreso geologico Argentino, San Miguel de Tucuman, Actas II, pp. 101–104.

Boyce, J.W., Hodges, K.V., 2005. U and Th zoning in Cerro de Mercado (Durango, Mexico) fluorapatite: insights regarding the impact of recoil redistribution of radiogenic 4He on (U-Th)/He thermochronology. Chem. Geol. 219, 261–274. https://doi.org/10.1016/j.chemgeo.2005.02.007.

Boyer, S., 1995. Sedimentary basin taper as a factor controlling the geometry and advance of thrust belts. Am. J. Sci. 295, 1220–1254.

Buelow, E.K., Suriano, J., Mahoney, J.B., Kimbrough, D.L., Mescua, J.F., Giambiagi, L.B., Hoke, G.D., 2018. Sedimentologic and stratigraphic evolution of the Cachueta basin: constraints on the development of the Miocene retroarc foreland basin. south-central Andes: Lithosphere 10 (3), 366–391. https://doi.org/10.1120/L709.1.

Butler, R.W., Bond, C.E., Cooper, M.A., Watkins, H., 2018. Interpreting structural geometry in fold-thrust belts: why style matters. J. Struct. Geol. 114, 251–273.
Capaldi, T.N., Horton, B.K., McKenzie, N.R., Stockli, D.F., Odlum, M.L., 2017. Sediment provenance in contractional orogens: the detrital zircon record from modern rivers in the Andean fold-thrust belt and foreland basin of western Argentina. Earth Planet Sci. Lett. 479, 83–97, 10 .1016/j.epsl .2017 .09 .001.
Capaldi, T.N., Horton, B.K., McKenzie, N.R., Mackaman-Lofland, C., Stockli, D.F., Ortiz, G., Alvarado, P., 2020. Neogene retroarc foreland basin evolution, sediment provenance, and magmatism in response to flat slab subduction, western Argentina. Tectonics 39, 1–29. https://doi.org/10.1029/2019TC005958.
Capaldi, T.N., McKenzie, N.R., Horton, B.K., Mackaman-Lofland, C., Colleps, C.L., Stockli, D.F., 2021. Detrital zircon record of Phanerozoic magmatism in the southern Central Andes. Geosphere 17, 876–897. https://doi.org/10.1130/ges02346.1.
Casquet, C., Baldo, E., Pankhurst, R.J., Rapela, C.W., Galindo, C., Fanning, C.M., Saavedra, J., 2001. Involvement of the Argentine Precordillera terrane in the Famatinian mobile belt: U-Pb SHRIMP and metamorphic evidence from. Sierra Pie de Palo: Geology 29 (8), 703–706.
Ciccioli, P.L., Marenssi, S.A., Amidon, W.H., Limarino, C.O., Kylander-Clark, A., 2018. Alluvial to lacustrine sedimentation in an endorheic basin during the mio-pliocene: the toro negro formation, central Andes of Argentina. J. S. Am. Earth Sci. 84, 69–87.
Coira, B.L., Davidson, J.D., Mpodozis, C., Ramos, V.A., 1982. Tectonic and magmatic evolution of the Andes of northern Argentina and Chile. Earth Sci. Rev. 18, 303–332. https://doi.org/10.1016/0012-8252(82)90042-3.
Collo, G., Davila, F., Teixeira, W., Nobile, J.C., Sant'Anna, L.G., Carter, A., 2017. Isotopic and thermochronologic evidence of extremely cold lithosphere associated with a slab flattening in the Central Andes of Argentina. Basin Res. 29, 16–40. https://doi.org/10.1111/bre.12162.
Contreras, V.H., Bracco, A.I., Baraldo, A, J., 2019. Estratigrafia, bioestratigrafia y cronologia del Mioceno superior de la provincia de San Juan (Argentina). Opera lilloana 52: Mioceno al Pleistoceno del centro y norte de Argentina p177–p206.
Coutts, D., Matthews, W.A., Hubbard, S.M., 2019. Assessment of widely used methods to derive depositional ages from detrital zircon populations. Geosci. Front. 10 (4), 1421–1435. https://doi.org/10.1016/j.gsf.2018.11.002.
Cristallini, E.O., Ramos, V.A., 2000. Thick-skinned and thin-skinned thrusting in the La ramada fold and thrust belt: crustal evolution of the high Andes of san juan, Argentina (32°SL). Tectonophysics 317, 205–235. https://doi.org/10.1016/S0040-1951(99)00276-0.
DeCelles, P.G., Burden, E.T., 1992. Non-marine sedimentation in the overfilled part of the Jurassic-Cretaceous Cordilleran foreland basin: morrison and Cloverly Formations, central Wyoming. USA: Basin Res. 4, 291–314. https://doi.org/10.1111/j.1365-2117.1992.tb00050.x.
DeCelles, P.G., Giles, K.A., 1996. Foreland basin systems. Basin Res. 8 (2), 105–123, 10.1046/j.1365-2117.1996.01491.x.
DeCelles, P.G., Gehrels, G.E., Quade, J., Ojha, T.P., Kapp, P.A., Upreti, B.N., 1998. Neogene foreland basin deposits, erosional unroofing, and the kinematic history of the Himalayan fold-thrust belt, western Nepal, 2 Geol. Soc. Am. Bull. 110 (1), 2–21. https://doi.org/10.1130/0016-7606(1998)110<0002:NFBDEU>2.3.CO.
Del Rey, A., Deckart, K., Arriagada, C., Martínez, F., 2016. Resolving the paradigm of the late Paleozoic–Triassic Chilean magmatism: isotopic approach. Gondwana Res. 37, 172–181. https://doi.org/10.1016/j.gr.2016.06.008.
Dickinson, W.R., Gehrels, G.E., 2009. Use of U–Pb ages of detrital zircons to infer maximum depositional ages of strata: a test against a Colorado Plateau Mesozoic database. Earth Planet Sci. Lett. 288 (1–2), 115–125. https://doi.org/10.1016/j.epsl.2009.09.013.
Ducea, M.N., Otamendi, J.E., Bergantz, G., Stair, K.M., Valencia, V.A., Gehrels, G., 2010. Timing constraints on building an intermediate plutonic arc crustal section. U-Pb zircon geochronology of the Sierra Valle Fértil–La Huerta, Famatinian arc, Argentina: Tectonics 29, TC4002. https://doi.org/10.1029/2009TC002615.
Elhers, T.A., Farley, K.A., 2003. Apatite (U-Th)/He thermochronometry: methods and applications to problems in tectonic and surface processes. Earth and Planetary Science Reviews 206, 1–14. https://doi.org/10.1016/S0012–821X(02)01069-5.
Erslev, E.A., 1993. Thrusts, back-thrusts, and detachment of Rocky Mountain foreland arches. In: Schmidt, C.J., Chase, R.B., Erslev, E.A. (Eds.), Laramide Basement Deformation in the Rocky Mountain Foreland of the Western United States, vol. 280. Geol. Soc. Am. Spec. Paper, pp. 339–358.
Farley, K.A., 2000. Helium diffusion from apatite: general behavior as illustrated by Durango fluorapatite. J. Geophys. Res. Solid Earth 105 (B2), 2903–2914.
Farley, K.A., 2002. U-Th)/He dating: techniques, calibrations, and applications. Rev. Mineral. Geochem. 47 (1), 819–844. https://doi.org/10.2138/rmg.2002.47.18.
Fernandez, A.E., Jordan, T.E., 1996. Analysis of Controls on Foreland Basin Stratigraphy Using Seismic and Outcrop Data: Application to the Bermejo Basin, Central Andes. Actas I. XIII Congreso Geologico Argentino y III Congreso de exploracion de hidrocarburos, Argentina, pp. 373–383.
Flemings, P.B., Jordan, T.E., 1989. A synthetic stratigraphic model of foreland basin development. J. Geophys. Res. 94, 3851–3866. https://doi.org/10.1029/JB094iB04p03851.
Flowers, R.M., Kelley, S.A., 2011. Interpreting data dispersion and "inverted" dates in apatite (U–Th)/He and fission-track datasets: an example from the US midcontinent. Geochem. Cosmochim. Acta 75 (18), 5169–5186.
Flowers, R.M., Ketcham, R.A., Shuster, D.L., Farley, K.A., 2009. Apatite (U-Th)/He thermochronometry using a radiation damage accumulation and annealing model. Geochem. Cosmochim. Acta 73, 2347–2365.
Flowers, R.M., Farley, K.A., Ketcham, R.A., 2015. A reporting protocol for thermochronologic modeling illustrated with data from the Grand Canyon. Earth Planet Sci. Lett. 432, 425–435.
Fosdick, J.C., Graham, S.A., Hilley, G.E., 2014. Influence of attenuated lithosphere and sediment loading on flexure of the deep-water Magallanes retroarc foreland basin, Southern Andes. Tectonics 33 (12), 2505–2525.
Fosdick, J.C., Carrapa, B., Ortíz, G., 2015. Faulting and erosion in the Argentine Precordillera during changes in subduction regime: reconciling bedrock cooling and detrital records. Earth Planet Sci. Lett. 432, 73–83. https://doi.org/10.1016/j.epsl.2015.09.041.
Fosdick, J.C., Reat, E.J., Carrapa, B., Ortiz, G., Alvarado, P.M., 2017. Retroarc basin reorganization and aridification during Paleogene uplift of the southern central Andes. Tectonics 36, 493–514. https://doi.org/10.1002/2016TC004400.
Furque, G., Gonzalez, P., Caballe, M., Perez, L., Cardo, R., Godeas, M., Conde, A., Pucci, J.C., 2003. Hoja Geológica 3169-II, San José de Jáchal. Provincias de San Juan y La Rioja. Instituto de Geología y Recursos Minerales, Servicio Geológico Minero Argentino, Buenos Aires. Boletín 259- 76.
Garzanti, E., Capaldi, T.N., Tripaldi, A., Zarate, M., Vezzoli, G., Limonta, M., 2022. Andean retroarc-basin dune fields and Pampean Sand Sea (Argentina): provenance and drainage changes driven by tectonics and climate. Earth Sci. Rev. 231 (4) https://doi.org/10.1016/j.earscirev.2022.104077.
Gehrels, G., 2014. Detrital zircon U-Pb geochronology applied to tectonics. Annu. Rev. Earth Planet Sci. 42, 127–149. https://doi.org/10.1146/annurev-earth-0502120124012.
González Bonorino, F., 1950. Algunos problemas geológicos de las Sierras Pampeanas. Rev. Asoc. Geol. Argent. 5 (3), 81–110.
Haschke, M., Günther, A., Melnick, D., Echtler, H., Reutter, K.J., Scheuber, E., Oncken, O., 2006. Central and southern Andean tectonic evolution inferred from arc magmatism. In: Oncken, O., et al. (Eds.), The Andes: Frontiers in Earth Sciences. Springer, Berlin, pp. 337–353, 10 .1007/978 -3 -540 -48684 -8_16.
Heredia, N., Fernández, L.R., Gallastegui, G., Busquets, P., Colombo, F., 2002. Geological setting of the Argentine Frontal Cordillera in the flat-slab segment (30° 00′–31° 30′ S latitude). J. S. Am. Earth Sci. 15 (1), 79–99.
Hervé, F., Fanning, C.M., Calderon, M., Mpodozis, C., 2014. Early Permian to late Triassic batholiths of the Chilean frontal cordillera (28-31 S): SHRIMP U-Pb zircon ages and Lu-Hf and O isotope systems. Lithos 184 (187), 436–446, 10.1016/j.Lithos.2013.10.018.
Horton, B.K., DeCelles, P.G., 2001. Modern and ancient fluvial megafans in the foreland basin systems of the central Andes, southern Bolivia: implications for drainage network evolution in fold-thrust belts. Basin Res. 13, 43–63.
Horton, B.K., Schmitt, J.G., 1996. Sedimentology of a lacustrine fan-delta system, Miocene horse camp formation. Nevada, USA: Sedimentology 43, 133–155. https://doi.org/10.1111/j.1365-3091.1996.tb01464.x.
Horton, B.K., Capaldi, T.N., Mackaman-Lofland, C., Perez, N.D., Bush, M.A., Fuentes, F., Constenius, K.N., 2022a. Broken foreland basins and the influence of subduction dynamics, tectonic inheritance, and mechanical triggers. Earth Sci. Rev., 104193
Horton, B.K., Capaldi, T.N., Perez, N.D., 2022b. The role of flat slab subduction, ridge subduction, and tectonic inheritance in Andean deformation. Geology 50 (9), 1007–1012.
Howard, J.L., 1993. The statistics of counting clasts in rudites: a review, with examples from the upper Palaeogene of southern California. USA: Sedimentology 40 (2), 157–174.
Jackson, S.E., Pearson, N.J., Griffin, W.L., Belousova, E.A., 2004. The application of laser ablation–inductively coupled plasma–mass spectrometry to in situ U-Pb zircon geochronology. Chem. Geol. 211, 47–69, 10.1016/j.chemgeo.2004.06.017.
Johnson, N., Jordan, T., Johnsson, P., Naser, C., 1986. Magnetic Polarity Stratigraphy, Age and Tectonic Setting of Fluvial Sediments in an Eastern Andean Foreland Basin, 1986. Foreland Basins, San Juan Province, Argentina, pp. 63–75.
Jones, R.E., Kirstein, L.A., Kasemann, S.A., Litvak, V.D., Poma, S., Alonso, R.N., Hinton, R., 2016. The role of changing geodynamics in the progressive contamination of Late Cretaceous to late Miocene arc magmas in the southern Central Andes. Lithos 262, 169–191, 10.1016/j.lithos .2016 .07 .002.
Jordan, T.E., 1995. Retroarc foreland and related basins. In: Busby, C.J., Ingersoll, R.V. (Eds.), Tectonics of Sedimentary Basins. Blackwell Science, pp. 331–362.
Jordan, T.E., Allmendinger, R.W., 1986. The Sierras Pampeanas of Argentina; a modern analogue of Rocky Mountain foreland deformation. Am. J. Sci. 286, 737–764. https://doi.org/10.2475/ajs.286.10.737.
Jordan, T.E., Isacks, B.L., Allmendinger, R.W., Brewer, J.A., Ramos, V.A., Ando, C.J., 1983. Andean tectonics related to geometry of subducted Nazca plate. Geol. Soc. Am. Bull. 94 (3), 341–361, 10.1130/0016-7606(1983)94<341: ATRTGO>2.0.CO;2.
Jordan, T.E., Rutty, P.M., McRae, L.E., Beer, J.A., Tabbutt, K., Damanti, J.F., 1990. Magnetic polarity stratigraphy of the Miocene Rio azul section, Precordillera thrust belt, san juan province, Argentina. J. Geol. 98, 519–539. https://doi.org/10.1086/629422.
Jordan, T.E., Allmendinger, R.W., Damanti, J.F., Drake, R.E., 1993. Chronology of motion in a complete thrust belt: the Precordillera, 30-31S, Andes mountains. J. Geol. 101, 135–156.
Jordan, T.E., Reynolds, J.H., Erikson, J.P., 1997. Variability in age of initial shortening and uplift in the Central Andes, 16-33S. In: Ruddiman, W. (Ed.), Tectonic Uplift and Climate Change. Plenum Press, New York, pp. 41–61.
Jordan, T.E., Schlunegger, F., Cardozo, N., 2001. Unsteady and spatially variable evolution of the Neogene Andean Bermejo foreland basin, Argentina. J. S. Am. Earth Sci. 14, 775–798.
Kay, S.M., Abbruzzi, J.M., 1996. Magmatic evidence for Neogene lithospheric evolution of the central Andean "flat-slab" between 30S and 32 S. Tectonophysics 259, 15–28. https://doi.org/10.1016/0040-1951(96)00032-7.
Kay, S.M., Coira, B.L., 2009. Shallowing and steepening subduction zones, continental lithospheric loss, magmatism, and crustal flow under the central Andean Altiplano-Puna Plateau. In: Kay, S.M., Ramos, V.A., Dickinson, W.R. (Eds.), Backbone of the

Americas: Shallow Subduction, Plateau Uplift, and Ridge and Terrane Collision. Geological Society of America Memoir 204, pp. 229–260. https://doi.org/10.1130/2009.1204(11.

Kay, S.M., Mpodozis, C., 2001. Magmatism as a probe to the Neogene shallowing of the Nazca plate beneath the modern Chilean flat- slab. J. S. Am. Earth Sci. 15, 39–57. https://doi.org/10.1016/s0895-9811(02)00005-6.

Kay, S.M., Mpodozis, C., Ramos, V.A., Munizaga, F., 1991. Magma source variations for mid-late Tertiary magmatic rocks associated with a shallowing subduction zone and a thickening crust in the central Andes (28 to 33°S). In: Harmon, R.S., Rapela, C.W. (Eds.), Andean Magmatism and its Tectonic Setting. Geological Society of America Special Paper 265, pp. 113–137, 10 .1130/SPE265 -p.113.

Keller, M., 1999. Argentine Precordillera: sedimentary and plate tectonic history of a Laurentian crustal fragment in South America. Geological Society of America 341, 1–131. https://doi.org/10.1130/0-8137-2341-8.1.

Ketcham, R.A., 2005. Forward and inverse modeling of low-temperature thermochronometry data. Rev. Mineral. Geochem. 58 (1), 275–314.

Kleiman, L.E., Japas, M.S., 2009. The Choiyoi volcanic province at 34°S–36°S (san rafael, mendoza, Argentina): implications for the late paleozoic evolution of the southwestern margin of gondwana. Tectonophysics 473 (3–4), 283–299, 10 .1016/j . tecto .2009 .02.046.

Kley, J., Monaldi, C.R., Salfity, J.A., 1999. Along-strike segmentation of the Andean foreland: causes and consequences. Tectonophysics 301, 75–94, 10 .1016/S0040-1951(98)90223-2.

Lacombe, O., Bellahsen, N., 2016. Thick-skinned tectonics and basement-involved fold-thrust belts: insights from selected Cenozoic orogens. Geol. Mag. 153, 763–810, 10.1017/S0016756816000078.

Lawton, T.F., Schellenbach, W.L., Nugent, A.E., 2014. Late Cretaceous fluvial-megafan and axial river systems in the southern cordilleran foreland basin: drip tank member of straight cliffs formation and adjacent strat. Southern Utah, U.S.A: J. Sediment. Res. 84, 407–434. https://doi.org/10.2110/jsr.2014.33.

Levina, M., Horton, B.K., Fuentes, F., Stockli, D.F., 2014. Cenozoic sedimentation and exhumation of the foreland basin system preserved in the Precordillera thrust belt (31-32°S), southern central Andes, Argentina. Tectonics 33, 1659–1680. https://doi.org/10.1002/2013TC003424.

Limarino, C., Tripalid, A., Marenssi, S., Net, L., Re, G., Caselli, A., 2001. Tectonic controls on the evolution of fluvial systems of the Vinchina Formation (Miocene), northwestern Argentina. J. S. Am. Earth Sci. 14, 751–762.

Löbens, S., Bense, F.A., Dunkl, I., Wemmer, K., Kley, J., Siegesmund, S., 2013. Thermochronological constraints of the exhumation and uplift of the Sierra de Pie de Palo, NW Argentina. J. S. Am. Earth Sci. 48, 209–219.

Lossada, A.C., Giambiagí, L., Hoke, G.D., Fitzgerald, P.G., Creixell, C., Murillo, I., Mardonez, D., Velasquez, R., Suriano, J., 2017. Thermochronologic evidence for late Eocene andean Mountain building at 30°S. Tectonics 36, 2693–2713. https://doi.org/10.1002/2017TC004674.

Mackaman-Lofland, C., Horton, B.K., Fuentes, F., Constenius, K.N., Stockli, D.F., 2019. Mesozoic to Cenozoic retroarc basin evolution during changes in tectonic regime, southern Central Andes (31–33 S): insights from zircon U-Pb geochronology. J. S. Am. Earth Sci. 89, 299–318.

Mackaman-Lofland, C., Horton, B.K., Fuentes, F., Constenius, K.N., Ketcham, R.A., Capaldi, T.N., Stockli, D.F., Ammirati, J.B., Alvarado, P., Orozco, P., 2020. Andean Mountain building and foreland basin evolution during thin- and thick-skinned Neogene deformation (32–33°S). Tectonics 39, 1–27. https://doi.org/10.1029/2019TC005838.

Mackaman-Lofland, C., Horton, B.K., Ketcham, R.A., McQuarrie, N., Fosdick, J.C., Fuentes, F., Constenius, K.N., Capaldi, T.N., Stockli, D.F., Alvarado, P., 2022. Causes of variable shortening and tectonic subsidence during changes on subduction: insights from flexural thermokinematic modeling of the Neogene southern central Andes (28-30S). Tectonics 41. https://doi.org/10.1029/2022tc007334.

Maksaev, V., Munizaga, F., Tassinari, C., 2014. Timing of the magmatism of the paleo-pacific border of gondwana: U-Pb geochronology of late paleozoic to early mesozoic igneous rocks of the north Chilean Andes between 20 and 30S. Andean Geol. 41, 447–506. https://doi.org/10.5027/andgeoV41n3-a01.

Malizia, D.C., Reynolds, J.H., Tabbutt, K., 1995. Cronología de la sedimentacion Neogena, tectonismo y edad de la estructuracion en el Campo de Talampaya, pp. 78–105.

Mardonez, D., Suriano, J., Giambiagi, L., Mescua, J., Lossada, A., Creixell, C., Murillo, I., 2020. The Jachal river cross-section revisited (Andes of Argentina, 30 S): constraints from the chronology and geometry of Neogene synorogenic deposits. J. S. Am. Earth Sci. 104, 10/1016/j.jsames.2020.102838.

Martin, E.L., Collins, W.J., Spencer, C.J., 2019. Laurentian origin of the Cuyania suspect terrane, western Argentina, confirmed by Hf isotopes in zircon. Geol. Soc. Am. Bull. 132, 273–290, 10 .1130/B35150 .1.

McGroder, M.F., Lease, R.O., Pearson, D.M., 2015. Along-strike variation in structural styles and hydrocarbon occurrences, Subandean fold-and-thrust belt and inner foreland, Colombia to Argentina. In: DeCelles, P.G., et al. (Eds.), Geodynamics of a Cordilleran Orogenic System: the Central Andes of Argentina and Northern Chile, vol. 212. Geological Society of America Memoir, pp. 79–113, 10 .1130/2015 .1212 (05).

Meigs, A., Krugh, W.C., Schiffman, C., Verges, J., Ramos, V.A., 2006. Refolding of the thin-skinned thrust sheers by active basement-involved thrust faults in the Eastern Precordillera of Western Argentina. Rev. Asoc. Geol. Argent. 61, 589–603.

Miall, A.D., 1977. Lithofacies types and vertical profile models in braided river deposits: a summary. In: Miall, A.D. (Ed.), Fluvial Sedimentology. Geological Survey of Canada, Calgary, pp. 597–604.

Miall, A.D., 1985. Architectural-element analysis: a new method of facies analysis applied to fluvial deposits. Earth Sci. Rev. 22 (4), 261–308.

Milana, J.P., Bercowski, F., Jordan, T.E., 2003. Paleoambientes y magnetoestrigrafía del Neógeno de la Sierra de Mogna, y su relación con la Cuenca de Antepaís Andina. Revista de la Associacion Geologica Argentina 38, 447–473.

Mpodozis, C., Kay, S.M., 1992. Late Paleozoic to Triassic evolution of the Gondwana margin: evidence from Chilean Frontal cordilleran batholiths (28°S to 31°S). Geol. Soc. Am. Bull. 104, 999–1014, 10.1130/0016-7606(1992)104<0999:LPTTEO>2.3.CO;2.

Mulcahy, S.R., Roeske, S.M., McClelland, W.C., Jourdan, F., Iriondo, A., Renne, P.R., Vervoort, J.D., Vujovich, G.I., 2011. Structural evolution of a composite middle to lower crustal section: the Sierra de Pie de Palo, northwest Argentina. Tectonics 30. https://doi.org/10.1029/2009TC002656.

Mulcahy, S.R., Roeske, S.M., McClelland, W.C., Ellis, J.R., Jourdan, F., Renne, P.R., 2014. Multiple migmatite events and cooling from granulite facies metamorphism within the Famatina arc margin of Northwest Argentina. Tectonics 33, 1–25, 10.1002/2013TC003398.

Nemec, W., Steel, R.J., 1984. Alluvial and coastal conglomerates: their significant features and some comments on gravelly mass-flow deposits, 10. In: Sedimentology of Gravels and Conglomerates. Canadian Society of Petroleum Geologists Memoir, Alberta, Canada, pp. 1–31.

Ortiz, G., Alvarado, P., Fosdick, J.C., Perucca, L., Saez, M., Venerdini, A., 2015. Active deformation in the northern Sierra de Valle Fértil, sierras Pampeanas, Argentina. J. S. Am. Earth Sci. 64, 339–350. https://doi.org/10.1016/j.jsames.2015.08.015.

Ortiz, G., Stevens Goddard, A.L., Fosdick, J.C., Alvarado, P., Carrapa, B., Cristofolini, E., 2021. Fault reactivation in the Sierras Pampeanas resolved across Andean extensional and compressional regimes using thermochronolgic modeling. J. S. Am. Earth Sci. 112 https://doi.org/10.1016/j.jsames.20210103533.

Otamendi, J.E., Ducea, M.N., Cristofolini, E.A., Tibaldi, A.M., Camilletti, G.C., Bergantz, G.W., 2017. U-Pb ages and Hf isotope compositions of zircons in plutonic rocks from the central Famatinian arc, Argentina. J. S. Am. Earth Sci. 76, 412–426. https://doi.org/10.1016/j.jsames.2017.04.005.

Paces, J.B., Miller, J.D., 1993. Precise U-Pb ages of duluth complex and related mafic intrusions, northeastern Minnesota: geochronological insights to physical, petrogenic, paleomagnetic and tectonomagmatic processes associated with the 1.1 Ga midcontinent rift system. J. Geophys. Res. Solid Earth 98, 13997–14013. https://doi.org/10.1029/93JB01159.

Parker, S.D., Pearson, D.M., 2021. Pre-thrusting stratigraphic control on the transition from a thin-skinned to thick-skinned structural style. An Example From the Double-Decker Idaho-Montana Fold-Thrust Belt: Tectonics 40. https://doi.org/10.1029/2020TC006429.

Paton, C., Hellstrom, J., Paul, B., Woodhead, J., Hergt, J., 2011. Iolite: freeware for the visualization and processing of mass spectrometric data. J. Anal. At. Spectrom. 26, 2508–2518.

Perez, N.D., Horton, B.K., 2014. Oligocene-Miocene deformational and depositional history of the Andean hinterland basin in the northern Altiplano plateau. Southern Peru: Tectonics 33, 1819–1847. https://doi.org/10.1002/2014TC003647.

Petrus, J.A., Kamber, B.S., 2012. VizualAge: a novel approach to laser ablation ICP-ms U-Pb geochronology data reduction. Geostand. Geoanal. Res. 36, 247–270.

Pfiffner, O.A., 2017. Thick-skinned and thin-skinned tectonics: a global perspective. Geosciences 7 (3), 71.

Pinto, L., Alarcón, P., Morton, A., Naipauer, M., 2018. Geochemistry of heavy minerals and U–Pb detrital zircon geochronology in the Manantiales Basin: implications for frontal cordillera uplift and foreland basin connectivity in the Andes of Central Argentina: palaeogeography, Palaeoclimatology. Palaeoecology 492, 104–125. https://doi.org/10.1016/j.palaeo.2017.12.017.

Podesta, M., Ortiz, G., Orozco, P., Alvarado, P., Fuentes, F., 2022. The Iglesia basin (San Juan, Argentina), seismic interpretation, geometry basin, and implications for geothermal systems. Andean Geol. 39 (3) https://doi.org/10.5027/andgeoV49n3-3340.

Ramos, V.A., 2004. Cuyania, an exotic block to Gondwana: review of a historical success and the present problems. Gondwana Res. 7, 1009–1026, 10.1016/S1342 -937X (05) 71081 -9.

Ramos, V.A., 2009. Anatomy and global context of the Andes: main geologic features and the Andean orogenic cycle. In: Kay, S.M., Ramos, V.A., Dickinson, W.R. (Eds.), Backbone of the Americas: Shallow Subduction, Plateau Uplift, and Ridge and Terrane Collision. Geological Society of America Memoir 204, pp. 31–65, 10 .1130/2009 .1204 (02).

Ramos, V.A., Folguera, A., 2009. Andean Flat-slab Subduction through Time, vol. 327. Geological Society, London, Special Publications, pp. 31–54. https://doi.org/10.1144/SP327.3.

Ramos, V.A., Jordan, T.E., Allmendinger, R.W., Kay, S.M., Cortes, J.M., Palma, M., 1986. Paleozoic terranes of the central Argentine-Chilean Andes. Tectonics 5, 855–880, 10 .1029/TC005i006p.00855.

Ramos, V.A., Vujovich, G.I., Cardó, R., Pérez, L., Pelichotti, R., Godeas, M., Pucci, J.C., Bercowski, F., Bordonaro, O., Chernicoff, Y.J., 2000. Hoja geologica 3169-IV, san juan. Provincia de San juan. Buenos Aires Servicio Geológico Minero Argentino. Instituto de Geología y Recursos Minerales. Boletín 243, 93.

Ramos, V.A., Cristallini, E.O., Pérez, D.J., 2002. The pampean flat-slab of the central Andes. J. S. Am. Earth Sci. 15, 59–78. https://doi.org/10.1016/S0895-9811(02)00006-8.

Rapela, C.W., Verdecchia, S.O., Casquet, C., Pankhurst, R.J., Baldo, E.G., Galindo, C., Murra, J.A., Dahlquist, J.A., Fanning, C.M., 2016. Identifying laurentian and SW gondwana sources in the neoproterozoic to early paleozoic metasedimentary rocks of the sierras Pampeanas: paleogeographic and tectonic implications. Gondwana Res. 32, 193–212, 10 .1016/j .gr .2015 .02 .010.

Rapela, C.W., Pankhurst, R.J., Casquet, C., Dahlquist, J.A., Fanning, C.M., Baldo, E.G., Galindo, C., Alasino, P.H., Ramacciotti, C.D., Verdecchia, S.O., Murra, J.A., 2018.

A review of the Famatinian Ordovician magmatism in southern South America: evidence of lithosphere reworking and continental subduction in the early proto-Andean margin of Gondwana. Earth Sci. Rev. 187, 259–285, 10.1016/j .earscirev .2018 .10 .006.

Rimando, J.M., Schoenbohm, L.M., 2020. Regional relative tectonic activity of structures in the Pampean flat slab segment of Argentina from 30 to 32 S. Geomorphology 350. https://doi.org/10.1016/j.geomorph.2019.106908.

Rubatto, D., 2017. Zircon. The Metamorphic Mineral: Rev. Mineral. Geochem. 83, 261–295. https://doi.org/10.2138/rmg.2017.83.09.

Sato, A.M., Llambías, E.J., Basei, M.A., Castro, C.E., 2015. Three stages in the late Paleozoic to Triassic magmatism of southwestern Gondwana, and the relationships with the volcanogenic events in coeval basins. J. S. Am. Earth Sci. 63, 48–69, 10.1016/j.jsames .2015 .07 .005.

Saylor, J.E., Jordan, J.C., Sundell, K.E., Wang, X., Wang, S., Deng, T., 2018. Topographic growth of the Jishi Shan and its impact on basin and hydrology evolution, NE Tibetan Plateau. Basin Res. 30, 544–563. https://doi.org/10.1111/bre.12264.

Schmitz, M.D., Bowring, S.A., 2001. U-Pb zircon and titanite systematics of the Fish Canyon Tuff: an assessment of high-precision U-Pb geochronology and its application to young volcanic rocks. Geochem. Cosmochim. Acta 65, 2571–2587. https://doi.org/10.1016/S0016-7037(01)00616-0.

Schwartz, J.J., Gromet, L.P., Miro, R., 2008. Timing and duration of the calc-alkaline arc of the Pampean orogeny: implications for the late Neoproterozoic to Cambrian evolution of western Gondwana. J. Geol. 116, 39–61, 10 .1086/524122.

Servicio Geológico Minero (SEGEMAR), 1999. Geologia Argentina: Buenos Aires, Argentina. SEGEMAR, scale 1:3,000,000, digital version, CD-ROM.

Servicio Geológico Minero (SEGEMAR), 2012. Sistema de Información Geográfica del Servicio Geológico Minero Argentino. Buenos Aires, Argentina, SEGEMAR, sig. segemar.gov.ar (accessed June 2018).

Servicio Nacional de Geología y Minería (Sernageomin), 2003. Mapa Geologico de Chile: version Digital. Sernageomin Publicación Geológica Digital 4 scale 1:1,000,000.

Shuster, D.L., Flowers, R.M., Farley, K.A., 2006. The influence of natural radiation damage on helium diffusion kinetics in apatite. Earth Planet Sci. Lett. 249, 148–161.

Siame, L.L., Bellier, O., Sebrier, M., Bourles, D.L., Leturmy, P., Perez, M., Araujo, M., 2002. Seismic hazard reappraisal from combined structural geology, geomorphology and cosmic ray exposure dating analyses: the Eastern Precordillera thrust system (NW Argentina). Geophys. J. Int. 150, 241–260.

Siame, L.L., Bellier, O., Sébrier, M., Araujo, M., 2005. Deformation partitioning in flat subduction setting: case of the Andean foreland of western Argentina (28°S-33°S). Tectonics 24, 1–24. https://doi.org/10.1029/2005TC001787.

Siame, L.L., Sébrier, M., Bellier, O., Bourlès, D., Costa, C., Ahumada, E.A., Gardini, C.E., Cisneros, H., 2015. Active basement uplift of Sierra Pie de Palo (Northwestern Argentina): rates and inception from10Be cosmogenic nuclide concentrations. Tectonics 34 (6), 1129–1153.

Sláma, J., et al., 2008. Plešovice zircon - a new natural reference material for U-Pb and Hf isotopic microanalysis. Chem. Geol. 249, 1–35. https://doi.org/10.1016/j.chemgeo.2007.11.005.

Smalley Jr., R., Pujol, J., Regnier, M., Chiu, J.M., Chatelain, J.L., Isacks, B.L., Araujo, M., Puebla, N., 1993. Basement seismicity beneath the Andean Precordillera thin-skinned thrust belt and implications for crustal and lithospheric behavior. Tectonics 12 (1), 63–76.

Sobel, E.R., Strecker, M.R., 2003. Uplift, exhumation and precipitation: tectonic and climatic control of Late Cenozoic landscape evolution in the northern Sierras Pampeanas. Argentina: Basin Res. 15 (4), 431–451. https://doi.org/10.1046/j.1365-2117.2003.00214.x.

Stevens-Goddard, A.S., Carrapa, B., Aciar, R.H., 2020. Recognizing drainage reorganization in the stratigraphic record of the Neogene foreland basin of the Central Andes. Sediment. Geol. 405, 105704.

Stevens-Goddard, A.L., Larrovere, M.A., Carrapa, B., Aciar, R.H., Alvarado, P., 2018. Reconstructing the thermal and exhumation history of the sierras Pampeanas through low-temperature thermochronology: a case study from the Sierra de Velasco. Geol. Soc. Am. Bull. 130 (11–12), 1842–1858. https://doi.org/10.1130/B31935.1.

Suriano, J., Mardonez, D., Mahoney, J.B., Mescua, J.F., Giambiagi, L.B., Kimbrough, D., Lossada, A., 2017. Uplift sequence of the Andes at 30 S: Insights from sedimentology and U/Pb dating of synorogenic deposits. J. S. Am. Earth Sci. 75, 11–34.

Tholt, A., Mulcahy, S., McClelland, W.C., Roeske, S.M., Meira, V.T., Webber, P., Houlihan, E., Coble, M.A., Vervoort, J.D., 2021. Metamorphism of the Sierra de Maz and implications for the tectonic evolution of the MARA terrane: Geosphere. https://doi.org/10.1130/GES02268.1.

Thomas, W.A., Astini, R.A., Mueller, P.A., McClelland, W.C., 2015. Detrital-zircon geochronology and provenance of the Ocloyic synorogenic clastic wedge, and Ordovician accretion of the Argentine Precordillera terrane. Geosphere 11, 1749–1769. https://doi.org/10.1130/GES01212.1.

Venerdini, A., Alvarado, P., Ammirati, J.B., Podesta, M., López, L., Fuentes, F., Linkimer, L., Beck, S., 2020. Crustal seismicity in the Andean Precordillera of Argentina using seismic broadband data. Tectonophysics 786, 228450.

Vergés, J., Ramos, E., Seward, D., Busquets, P., Colombo, F., 2001. Miocene sedimentary and tectonic evolution of the Andean Precordillera at 31°S, Argentina. J. S. Am. Earth Sci. 14 (7), 735–750, 10.1016/S0895- 9811(01)00070-0.

Vergés, J., Ramos, V.A., Meigs, A., Cristallini, E., Bettini, F.H., Cortés, J.M., 2007. Crustal wedging triggering recent deformation in the Andean thrust front between 31°S and 33°S: sierras Pampeanas-Precordillera interaction. J. Geophys. Res. Solid Earth 112, 1–22. https://doi.org/10.1029/2006JB004287.

Vermeesch, P., 2018. IsoplotR: a free and open toolbox for geochronology. Geosci. Front. 9, 1479–1493. https://doi.org/10.1016/j.gsf.2018.04.001.

Von Gosen, W., 1992. Structural evolution of the Argentine Precordillera: the Rio san juan section. J. Struct. Geol. 14, 643–667. https://doi.org/10.1016/0191-8141(92)90124-F.

Vujovich, G.I., van Staal, C.R., Davis, W., 2004. Age constraints on the tectonic evolution and provenance of the Pie de Palo complex, Cuyania composite terrane, and the famatinian orogeny in the Sierra Pie de Palo, san juan, Argentina. Gondwana Res. 7, 1041–1056.

Yáñez, G.A., Ranero, C.R., Huene, R., Díaz, J., 2001. Magnetic anomaly interpretation across the southern Central Andes (32–34 S): the role of the Juan Fernández ridge in the late tertiary evolution of the margin. J. Geophys. Res. 106 (B4), 6325–6345. https://doi.org/10.1029/2000JB900337.

Zapata, T.R., 1998. Crustal structure of the Andean thrust front at 30 S latitude from shallow and deep seismic reflection profiles, Argentina. J. S. Am. Earth Sci. 11 (2), 131–151.

Zapata, T.R., Allmendinger, R.W., 1996. Thrust-front zone of the Precordillera, Argentina: a thick-skinned triangle zone. AAPG (Am. Assoc. Pet. Geol.) Bull. 80, 359–381. https://doi.org/10.1306/64ed87e6-1724-11d7-8645000102c1865d.